JCI The Journal of Clinical Investigation

Profilin1 delivery tunes cytoskeleton dynamics towards CNS axon regeneration

Rita Pinto-Costa, … , Reinhard Fässler, Monica M. Sousa

J Clin Invest. 2020. https://doi.org/10.1172/JCI125771.

Research In-Press Preview Cell biology Neuroscience

Graphical abstract

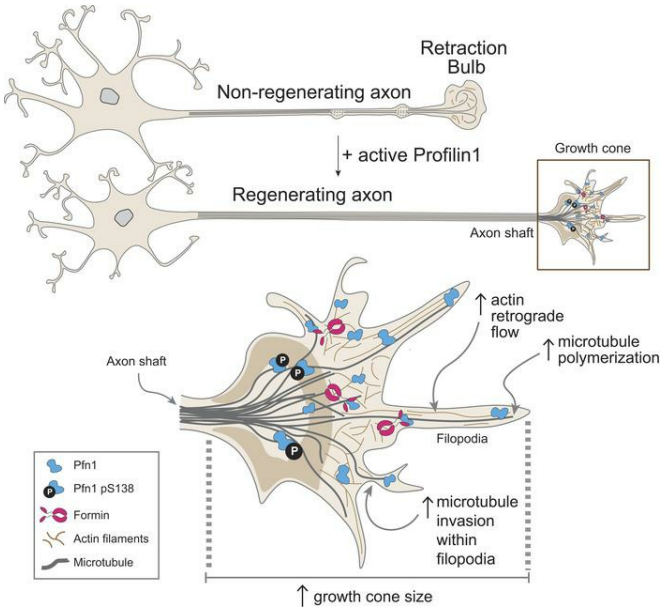

Profilin1 delivery tunes cytoskeleton dynamics towards CNS axon regeneration

Rita Pinto-Costa,[1,3] Sara C. Sousa,[1,3] Sérgio C. Leite,[1] Joana Nogueira-Rodrigues,[1,3] Tiago Ferreira da Silva,[2] Diana Machado,[1] Joana Marques,[1] Ana Catarina Costa,[1] Márcia A. Liz,[1] Francesca Bartolini,[4] Pedro Brites,[2] Mercedes Costell,[5] Reinhard Fässler,[6] and Mónica M. Sousa[1]

[1]Nerve Regeneration Group and [2]NeuroLipid Biology Group, Program in Neurobiology and Neurologic Disorders, Instituto de Biologia Molecular e Celular – IBMC and Instituto de Inovação e Investigação em Saúde, Universidade do Porto, 4200-135 Porto, Portugal.

[3]Graduate Program in Molecular and Cell Biology, Instituto de Ciências Biomédicas Abel Salazar- ICBAS, University of Porto, 4050-313 Porto, Portugal.

[4]Department of Pathology and Cell Biology, Columbia University, New York, NY 10032, USA.

[5]Department of Biochemistry and Molecular Biology and Estructura de Reserca Interdisciplinar en Biotecnologia i Biomedicina, Universitat de València, 46100 Burjassot, Spain.

[6]Max Plank Institute of Biochemistry, Department of Molecular Medicine, Max Plank Institute of Biochemistry, 82152 Martinsried, Germany.

Conflict of interest: The authors have declared that no conflict of interest exists.

Address correspondence to: Mónica Mendes Sousa, Nerve Regeneration Group, Program in Neurobiology and Neurologic Disorders, Instituto de Biologia Molecular e Celular – IBMC and Instituto de Inovação e Investigação em Saúde, Universidade do Porto, Rua Alfredo Allen 208, 4200-135 Porto, Portugal. Phone: +351 220 408 800; E-mail: msousa@ibmc.up.pt

Abstract

After trauma, regeneration of adult CNS axons is abortive causing devastating neurologic deficits. Despite progress in rehabilitative care, there is no effective treatment stimulating axon growth following injury. Using models with different regenerative capacities, followed by gain- and loss-of-function analysis, we identified profilin1 (Pfn1) as a coordinator of actin and microtubules (MTs), powering axon growth and regeneration. In growth cones, Pfn1 increased actin retrograde flow, MT growth speed and invasion of filopodia by MTs, orchestrating cytoskeleton dynamics towards axon growth. In vitro, active Pfn1 promoted MT growth in a formin-dependent manner, whereas localization of MTs to growth cone filopodia was facilitated by direct MT-binding and interaction with formins. In vivo, Pfn1 ablation limited regeneration of growth-competent axons after sciatic nerve and spinal cord injury. Adeno-associated viral (AAV) delivery of constitutively active Pfn1 to rodents promoted axon regeneration, neuromuscular junction maturation and functional recovery of injured sciatic nerves, and increased the ability of regenerating axons to penetrate the inhibitory spinal cord glial scar. Thus, we identify Pfn1 as an important regulator of axon regeneration and suggest that AAV-mediated delivery of constitutively active Pfn1, together with the identification of modulators of Pfn1 activity, should be considered to treat the injured nervous system.

Keywords: axonal cytoskeleton, axon growth, axon regeneration, profilin, spinal cord injury.

Introduction

In the adult CNS, developmental axon growth capacity declines such that regeneration after injury is abortive. This derives from the highly inhibitory environment formed at the injury site, and the inability of CNS neurons to activate a cell-intrinsic pro-regenerative program (1). However, it is possible to stimulate the intrinsic growth capacity of specific CNS axons. In sensory dorsal root ganglia (DRG) neurons, which bear two axonal branches with different structure and function (2), upon injury of the peripheral axon (conditioning lesion – CL), the central axon gains growth competence and regenerates within the inhibitory CNS milieu (3). Using this elegant model, several regeneration-associated genes and transcription factors that promote axon regrowth were unveiled (1). In recent years, cytoskeleton organization and dynamics, specially actin and MTs, have emerged as key players in axon growth and regeneration (4). In particular, cytoskeleton modulation at the axon tip can power the formation of a competent growth cone from a dystrophic growth-incompetent retraction bulb, promoting regeneration of CNS axons (4).

The peripheral domain of the growth cone is highly enriched in actin (5), a multifunctional cytoskeleton component regulated by numerous actin-binding proteins. Actin presents as either a free globular monomer – G-actin – or as part of a filament – F-actin – both of which are essential for its various functions. Cyclic polymerization and depolymerization of actin filaments in the growth cone is needed to generate the mechanical force that prompts axon elongation (6, 7). Local actin instability specifies neuronal polarization and axon formation. Consistently, actin-depolymerizing drugs and Rho-inactivators, that act upon the actin cytoskeleton, generate neurons with multiple axons (6). RhoA signaling is a central mediator of inhibitory cascades hindering axon regeneration (8-10). In this context, RhoA inhibitors improve axon regeneration (11, 12) and are currently used in clinical trials aimed at treating spinal cord injury (13). Nevertheless, the interplay between different actin-binding proteins controlling actin dynamics in the growth cone is still not well understood. The actin-binding and -severing protein cofilin1 (Cfl1) (14) for example,

is essential for actin remodeling during neurite formation (15). Cfl synergizes with the G-actin-binding and actin polymerization-promoting protein profilin (Pfn) to further enhance the rate of actin filament treadmilling (16). Although Cfl has been involved in powering axon extension (17), growth cone turning during axon pathfinding (18) and axon regeneration (19), the role of Pfn on mammalian axon growth has been less explored.

In mammals, the profilin family consists of the ubiquitously expressed Pfn1, the brain-specific Pfn2 and the testis-specific Pfn3 and Pfn4. Globally, profilins act as nucleation/polymerization-inhibiting G-actin sequestering molecules (20), which turn into elongators through interaction with either Ena/VASP or formins (21, 22). Although Pfn1 and Pfn2 are expressed in the brain, their specific role in neurons needs to be further explored. Whereas actin polymerization in neurons may be mainly regulated by Pfn1, neuronal Pfn2 seems to be specifically associated to synaptic plasticity (23). In addition to their role as regulators of actin dynamics, profilins may also influence MT organization (24-26). Mutations in Pfn1 have been associated to neurodegenerative diseases including amyotrophic lateral sclerosis (ALS), supporting Pfn1 relevance in neuron architectural biology. Apart from binding actin, profilins also interact with poly-proline stretches in proteins (which are present in a vast majority of actin-binding proteins) (27), and with phosphatidylinositol 4,5-bisphosphate (PIP2) (28), which links Pfn to the plasma membrane. Given the heterogeneous nature of Pfn ligands, profilins participate in several biological processes, acting as intracellular multifunctional platforms.

Here we unveil Pfn1 as a novel pro-regenerative molecule that promotes actin and MT cytoskeleton crosstalk in actively growing axon terminals. Our results identify Pfn1 as a central regulator of axon growth and regeneration and suggest new therapeutic strategies to promote axon regrowth, specifically by interfering with Pfn1 levels and activity.

Results

Pfn1 activity increases after conditioning lesion. Given the robustness of a CL in axon growth and regeneration (3), and the importance of actin dynamics in the growth cone for axon elongation (6), we determined how CL influences actin dynamics. For that, we analysed adult DRG neurons under two distinct growth modes (29): naïve and regenerative growth (i.e., the growth mode resulting from a previous CL). The sciatic nerve (containing peripheral branches of DRG neurons) was lesioned in vivo (Figure 1A), and DRG were collected 1 week later for in vitro culture. In cultured DRG neurons, CL increased actin dynamics in the growth cone, promoting actin retrograde flow (Figure 1, B-D), similarly to recent observations (19). In addition, CL growth cones showed increased area (Figure 1, B and E) and displayed a substantial accumulation of Pfn1 (Figure 1, F and G), raising the possibility that this protein might be important for actin dynamics in the axonal tip, and for growth competence. Next, we investigated the regulation of Pfn1 in vivo by comparing its levels following both spinal cord injury (SCI, a non-regenerative condition) and CL (a high regenerative condition) (Figure 1A). The levels of Pfn1 were increased in DRG after CL, supporting a global increase in expression (Figure 1, H and I). Moreover, the total levels of Pfn1 increased 7-fold at the injury site of rats with CL versus SCI, suggesting that it accumulates distally in growth cones (Figure 1, J and K). Given that glial or myeloid cells might contribute to the effect observed in spinal cord extracts, the specific upregulation of Pfn1 in axons was assessed by immunofluorescence. In animals with CL, Pfn1 was specifically detected in the spinal cord, in growth cones labeled by SCG10, a stathmin preferentially expressed in regenerating sensory axons (30) (Figure 1L), in accordance with our in vitro findings in growth cones of conditioned neurons (Figure 1, F and G). Non-phosphorylated Pfn1 is the active form of the protein; its activity can be downregulated by RhoA/ROCK-mediated phosphorylation at serine 138 (31). Importantly, in addition to increased Pfn1 levels, CL induced an 8.6-fold downregulation of the serine 138 phosphorylation of Pfn1 (Figure 1, J and K), thus increasing levels of the Pfn1 active form. In line with this finding, ROCK1, a central axon growth inhibitory molecule (32), was also 2.5-fold decreased following CL (Figure 1, J and K). Importantly, the levels of Pfn2

were not altered by CL (Figure 1, J and K), suggesting a Pfn1-specific effect. Collectively, these data support that Pfn1 is an important pro-regenerative regulator of actin dynamics in the growth cone.

Pfn1 downregulation impairs axon growth in different neuron types and developmental stages. To test the hypothesis that Pfn1 levels promote axon growth capability, we silenced Pfn1 in cultured adult DRG neurons under naïve (Figure 2, A and B) and regenerative growth (i.e., following from a previous CL) conditions (Figure 2, C and D). In naïve DRG neurons, Pfn1 knockdown (> 80% efficiency both in DRG and hippocampal neuron cultures) led to a 30% reduction in neurite length and to reduced branching when compared with DRG neurons nucleofected with an empty control plasmid (CTR) (Figure 2, E and F). The specificity of these effects was confirmed by expressing a human shRNA-resistant version of WT hPfn1 (WT hPfn1*), which reverted the analysed parameters to normal levels (Figure 2, E and F). Downregulation of Pfn1 had an even more pronounced effect in conditioned DRG neurons i.e., after activating the regenerative growth mode (CL), reducing by 44% neurite elongation (Figure 2, C-F). Together, our results suggest that Pfn1 is a key mediator of growth after CL. To extend our findings to additional neuron types, we silenced Pfn1 in hippocampal neurons. When lentivirus-mediated delivery of shRNA against Pfn1 was performed, the majority of hippocampal neurons were arrested in stage 1, lacking neurite-like processes (Figure 2, G and H). When shRNA plasmids were delivered through nucleofection to DIV0 hippocampal neurons, neuronal polarization was delayed, resulting in an increase of 2.3- and 1.4- fold of stage 1 and stage 2 neurons, respectively (Figure 2, I and J). Similarly to naïve DRG neurons, hippocampal neurons that were able to polarize had an approximately 24% reduction in axon length (Figure 2K) and dendritic growth was reduced by over 27% (Figure 2L).

In vivo *depletion of Pfn1 curbs axon regeneration in the peripheral and central nervous system.* To determine if our in vitro findings can be extended to an in vivo system,

we developed an inducible neuron-specific Pfn1 knockout mouse model using *Cre-loxP* technology. In this model, the yellow fluorescent protein (YFP) is co-expressed with inducible-CreER^{T2} (Figure 3A) and a high percentage of DRG axons in cre^{+}Pfn1 sciatic nerves is YFP-positive (Supplemental Figure 1A). Pfn1 levels were severely decreased in brain samples of cre^{+}Pfn1$^{fl/fl}$ mice when compared to cre^{+}Pfn1$^{wt/wt}$ controls, whereas levels of Pfn2 remained normal (Supplemental Figure 1, B-D). Importantly, and in line with the in vitro acute shRNA-mediated knockdown, the permanent absence of Pfn1 from naïve DRG neurons of adult cre^{+}Pfn1$^{fl/fl}$ mice significantly impaired neurite length (55% reduction) and branching (Figure 3, B-D). Given the structural and possible functional similarities between the ubiquitous Pfn1 and brain-specific Pfn2, we investigated if Pfn2 would also regulate neurite outgrowth in DRG neurons. Interestingly, downregulation of Pfn2 levels (Supplemental Figure 1, E and F) decreased neuronal growth cone area although to a lower extent than that of Pfn1 (Supplemental Figure 1, G and H). However, Pfn2 downregulation did not change the elongation competence or branching of either cre^{+}Pfn1$^{wt/wt}$ or cre^{+}Pfn1$^{fl/fl}$ naïve DRG neurons (Figure 3, B-D). These observations suggest that brain-specific Pfn2 might play alternative functions in DRG neurons, unrelated to neurite growth.

Next, we determined whether the lack of Pfn1 is sufficient to impair axon regeneration in vivo in two well-described paradigms leading to robust axon regeneration: the sciatic nerve injury and the CL model. Following sciatic nerve injury, axons successfully regenerate and remyelination occurs soon after injury. Upon crushing the sciatic nerve we counted myelinated axons distally to the lesion site at different time points (Figure 3E). At 7 days post-injury the density of myelinated fibers in cre^{+}Pfn1$^{fl/fl}$ mice showed an over 40% decrease tendency in comparison to cre^{+}Pfn1$^{wt/wt,}$ mice, and at 15 days post-injury the absence of Pfn1 led to a significant decrease in the number of myelinated axons (Figure 3, F and G). These results indicate an impaired axon regeneration capacity in the absence of Pfn1 in vivo. Of note, no differences in remyelination were detected in cre^{+}Pfn1$^{fl/fl}$ mice, as assessed by g-ratio measurements at 15 and 28 days post-injury (data not shown). At 28 days post-injury, functional synaptic contacts – neuromuscular junctions (NMJs) – in the gastrocnemius

muscle were evaluated through the analysis of acetylcholine receptor (AChR) clusters, using the postsynaptic marker bungarotoxin. Analysis of 3D-surface reconstructed AChR clusters revealed that the structural volume and complexity were largely reduced in cre^{+}Pfn1$^{fl/fl}$ mice (Figure 3, H-J), pointing towards a delayed NMJ maturation in the absence of Pfn1. At the functional level, motor nerve conduction velocity showed a clear deficit in cre^{+}Pfn1$^{fl/fl}$ mice compared with cre^{+}Pfn1$^{wt/wt}$ mice (Figure 3K), supporting a decreased number of functional myelinated axons. Together these results support that the lack of Pfn1 results in defective axon regeneration and functional recovery of damaged peripheral axons.

We also used the CL paradigm as an alternative in vivo model. In this experimental model, the enhanced regenerative capacity of the ascending dorsal column tract was assessed in mice, in which a sciatic nerve transection preceded an acute spinal cord lesion (dorsal hemisection) (Figure 3L). Cholera toxin B (CT-B) subunit, a tracer previously injected in the sciatic nerve, was used to visualize regenerating dorsal column ascending sensory axons (Figure 3M). The injured dorsal column tract was clearly identified by the accumulation of YFP expressing axons in the dorsal region of the thoracic spinal cord (Figure 3M). Whereas dorsal column tract axons (yellow, highlighted with white arrowheads), accumulated in the lesion border of cre^{+}Pfn1$^{wt/wt}$ mice with SCI (Figure 3M, upper panel), long distance regeneration (4.4-fold increase) was observed in cre^{+}Pfn1$^{wt/wt}$ mice with CL (Figure 3M, middle panel). In sharp contrast, cre^{+}Pfn1$^{fl/fl}$ mice with CL showed over 50% reduction in the mean regenerating distance (Figure 3M, bottom panel), with most axons already aborting their regeneration close to the injury border (Figure 3, M and N). As an internal control, CT-B^{+}YFP^{-} axons were measured, further supporting a Pfn1-specific effect (Figure 3N) in regulating axonal regeneration. These observations support that Pfn1 is an important player for optimal axon extension after injury in vivo.

Pfn1 regulates actin and MT dynamics in the growth cone, increasing axon growth in vitro. Since the force required to power axon growth and regeneration is regulated by cytoskeletal components at the distal tip of a growing neurite, we compared cytoskeleton

dynamics in growth cones of adult DRG neurons from cre^{+}Pfn1$^{wt/wt}$ and cre^{+}Pfn1$^{fl/fl}$ mice. Phalloidin staining revealed that cre^{+}Pfn1$^{fl/fl}$ sensory neurons extended smaller growth cones (Figure 4, A and B), in support of our data using shRNA-mediated downregulation of Pfn1 in hippocampal neurons (Supplemental Figure 1, G and H). Although we observed a similar number of filopodia in cre^{+}Pfn1$^{fl/fl}$ and cre^{+}Pfn1$^{wt/wt}$ animals (Figure 4, A and C), the existing filopodia in cre^{+}Pfn1$^{fl/fl}$ growth cones were significantly shorter compared to controls (Figure 4, A and D). Furthermore, actin dynamics assessed by measuring the velocity of actin retrograde flow, was reduced by 30% in growth cones of adult cre^{+}Pfn1$^{fl/fl}$ DRG neurons (Figure 4, E-G) and was reverted upon re-expression of WT hPfn1 (Figure 4, E-G). Interestingly, in addition to actin dynamics, MT growth speed, measured in growth cone filopodia, was also affected by Pfn1 deletion. In cre^{+}Pfn1$^{fl/fl}$ DRG neurons, the end-binding protein 3 (EB3) comet speed was 50% diminished (Figure 4, H-J), with growing MTs presenting a decreased growth length (Supplemental Figure 2A), without a significant difference in the duration of growth (Supplemental Figure 2B). The defect in MT dynamics in cre^{+}Pfn1$^{fl/fl}$ DRG neurons was completely reverted by the expression of WT hPfn1 (Figure 4, H-J). Of note, when similar analyses were performed in the axon shaft, Pfn1 deletion did not affect significantly EB3 comet speed (Figure 4J), supporting a possible compartment-specific function of Pfn1 in the growth cone**.** Combined, these data suggest that in the absence of Pfn1, MTs polymerize at lower rates likely leading to shorter MTs. Similar results were obtained in growth cones of embryonic hippocampal neurons, which also showed over 25% decreased actin retrograde flow upon shRNA-mediated knockdown of Pfn1 (Supplemental Figure 2, C-E), and significantly reduced growth speed and length of polymerizing MTs onto the peripheral membrane edge (Supplemental Figure 2, F-I). Of note, in these live-cell experiments, fluorescently tagged LifeAct and EB3 were imaged in growth cones of stage 3 hippocampal neurons. However, a considerable number of stage 1 neurons was consistently observed in the shRNA Pfn1 condition (Supplemental Figure 2, C and F, middle panel). Thus, acute Pfn1 depletion induced defective actin and MT dynamics, which in many neurons led to an arrest of axon outgrowth.

The CL model suggests that an increased activity of Pfn1 is necessary to achieve a high-regenerative capacity (Figure 1). Therefore, we hypothesized that the delivery of active Pfn1 might persistently accelerate cytoskeleton dynamics in the growth cone ultimately leading to axon elongation. To test this hypothesis, we generated a constitutively active non-phosphorylatable Pfn1 mutant (S138A hPfn1). In adult sensory DRG neurons, overexpression of S138A hPfn1 elicited a 2.6-fold increase in total neurite length (Figure 4, K and L) and a substantial rise in the mean number of branches (Figure 4M) whereas only a small increase in both parameters was observed upon overexpression of WT hPfn1. Of note, overexpression efficiency was similar for both WT hPfn1 and S138A hPfn1 (Supplemental Figure 2, J and K). Importantly, S138A hPfn1 was also effective in promoting growth (1.4-fold increase) of adult DRG neurons cultured on inhibitory substrates such as aggrecan (Figure 4N). This data demonstrates that active Pfn1 is an important enhancer of axon growth under permissive as well as inhibitory conditions. Since Pfn1-depleted neurons show abnormal cytoskeleton dynamics in their growth cones, we hypothesized that increased Pfn1 activity may promote not only actin but also MT dynamics. In support of our hypothesis, overexpression of both WT and S138A hPfn1 significantly increased actin retrograde flow (Figure 4, O-Q) and EB3 comet speed (Figure 4, R-T) at the growing tip, with S138A hPfn1 presenting a significantly higher effect. Importantly, similar results were obtained in hippocampal neuron cultures, suggesting that S138A hPfn1 affects these parameters in different neuronal populations. Specifically, S138A hPfn1 expressing DIV4 hippocampal neurons presented longer axons (Supplemental Figure 2, L and M) and increased actin (Supplemental Figure 2N) and MT dynamics (Supplemental Figure 2, O and P). Together, our data suggests that S138A hPfn1 is a robust activator of actin and MT dynamics in the growth cone, and of axon growth capacity.

Regulation of the MT cytoskeleton in growth cones and promotion of axon elongation by S138A hPfn1 are facilitated by direct MT binding and interaction with formins. Pfn1 has a plethora of ligands, including actin, poly-proline-containing proteins and PIP2 at the plasma

membrane (28) (Figure 5A). In addition to the above ligands, Pfn1 is able to bind directly to MTs in vitro (25), through residues found mutated in ALS patients, including G118 (Figure 5A) (33). Given this evidence, we explored the possibility that in neurons, S138A hPfn1 might increase MT growth speed through direct binding to MTs. For that, we expressed in hippocampal neurons the MT binding-deficient G118V hPfn1 (25, 33) in a constitutively active S138A hPfn1 backbone (G118V/S138A hPfn1). Of note, the speed of actin retrograde flow in growth cones is still powered by the expression of G118V hPfn1 (Supplemental Figure 2, Q-S), allowing to uncouple the effect of this mutant on MT growth from a possible effect on actin dynamics. Interestingly, expression of the double mutant G118V/S138A hPfn1, increased MT growth speed to a comparable extent as the single mutant S138A hPfn1 (Figure 5, B-D). Thus, S138A hPfn1 increases MT growth through a mechanism that does not involve direct MT binding. To understand if Pfn1 molecular partners participate on the effect of constitutively active Pfn1 in MT dynamics, we explored the relevance of the Pfn1 poly-proline binding domain. Overexpression of the double mutant H134S/S138A hPfn1 i.e., poly-proline binding-deficient hPfn1, decreased S138A hPfn1 ability to promote MT growth speed (Figure 5, B-D). This data supports the notion that in growth cones, S138A hPfn1 increases MT dynamics through a poly-proline-containing partner. Pfn1 works closely with formins that bear a proline-rich formin homology domain 1 (FH1) and function as actin assembly factors assisting the formation of unbranched actin filaments (34). Whereas FH1 speeds actin assembly by recruiting Pfn-bound actin monomers to the vicinity of the barbed end through its proline-rich motifs, the formin homology domain 2 (FH2), after nucleating actin dimers, remains attached to the actin filament to assist its elongation (35). In addition to regulating actin filament growth, formins also bind MTs and influence their stability independently of actin binding (36, 37). We analysed if formins might mediate the effect of S138A hPfn1 in promoting MT growth speed in neuronal growth cones. Inhibition of formins with a small molecule inhibitor of the FH2 domain (SMIFH2) (38), was sufficient to prevent constitutively active S138A hPfn1 of powering MT growth speed (Figure 5, B-D). Thus, our

data show that S138A hPfn1 increases MT dynamics through a formin-dependent mechanism.

In the central domain of the growth cone, axonal MT bundles terminate and few explorative MTs enter within filopodia of the growth cone peripheral domain. These MTs can lead the advance of the shaft MT bundles, culminating in axon growth (7, 39-41). Given this evidence, to further dissect the effect of Pfn1 in the growth cone, we assessed filopodia invasion by MTs. Constitutively active S138A hPfn1 strongly enhanced the localization of growing MTs to growth cone filopodia (Figure 5E). This effect was sharply diminished when direct Pfn1 binding to MTs was abolished through the use of the double mutant G118V/S138A hPfn1 and was totally reverted by a poly-proline-binding deficient mutant (H134S/S138A hPfn1) or inhibition of formins (Figure 5E). Taken together, our data show that S138A hPfn1 increases MT growth speed through a formin-dependent mechanism, whereas localization of growing MTs to filopodia is promoted both through direct MT binding and interaction with formins. In line with the above findings, the ability of constitutively active Pfn1 to promote axon growth was severely impaired by a mutation either on MT-binding (G118V/S138A hPfn1) or on poly-proline-binding region of S138A hPfn1 (H134S/S138A hPfn1), and by formin inhibition (Figure 5, F and G). Interestingly, abolishing both direct MT binding and formin interaction (G118V/S138A hPfn1+SMIFH2 treatment) showed a tendency for a cumulative negative effect in axon growth (Figure 5, F and G). In summary, our data shows that the capacity of specific Pfn1 residues to mediate MT invasion of growth cone filopodia (even more than their ability to enhance MT growth speed), correlates with their effect in the regulation of axon growth.

In vivo delivery of S138A hPfn1 efficiently promotes regeneration of peripheral and CNS axons. In the adult CNS, following the establishment of connections, axons mostly fail to regenerate after injury or disease. Our data demonstrates that S138A hPfn1 is a novel and potent pro-regenerative molecule, capable of enhancing axon growth in vitro both under permissive and inhibitory conditions. As a proof-of-concept, to further disclose its

regenerative potential, we delivered S138A hPfn1 and the poly-proline binding-deficient mutant H134S/S138A hPfn1 in mice before either sciatic nerve injury or SCI. In order to easily trace Pfn1 expressing axons in vivo, we generated bicistronic expression vectors encoding enhanced GFP linked to S138A hPfn1 via the 2A self-cleaving small peptide (P2A), and packaged them into adeno-associated viral (AAV) particles containing the PHP.eB capsid, that allow non-invasive gene delivery to the nervous system (42). CAD cell extracts show that cells transfected with pAAV.GFP.P2A.S138A hPfn1 and pAAV.GFP.P2A.H134S/S138A hPfn1 plasmids present similar levels of overexpressed mutant Pfn1 (Supplemental Figure 3, A and B). In vivo, two weeks following viral administration through the tail vein, GFP expression was clearly detected throughout mouse brain, DRG and spinal cord neurons (Supplemental Figure 3, C-E). To evaluate the in vivo regeneration capacity of peripheral axons expressing S138A hPfn1 or H134S/S138A hPfn1, AAVs were injected in the tail vein and 15 days later, sciatic nerves were crushed at the thigh level, allowing to persistently define the crush site (Figure 6A). Three days after injury, in mice where pAAV.GFP.P2A.S138A hPfn1 was delivered, peripheral sensory axons regenerated over significantly longer distances than those of controls, as assessed both by SCG10 staining (Figure 6, B and C) and by measuring the distance of GFP^+ axons from the lesion border in which case almost 2-fold longer axons were found (Figure 6D). In contrast, when H134S/S138A hPfn1 i.e., the constitutively active Pfn1 mutant lacking the ability to bind poly-proline-containing proteins was delivered, the robust regenerative effect of S138A hPfn1 was substantially reduced (Figure 6 B-D) and the distance of GFP^+ axons to the lesion boarder was indistinguishable from that of control AAV-GFP expressing axons (Figure 6D). At 28 days post-injury, increased levels of active Pfn1 improved NMJ maturation; NMJs from S138A hPfn1 expressing animals presented a structural volume and complexity similar to that of the uninjured control group (Figure 6, E-G). In contrast, in AAV-GFP injected animals NMJs were not yet fully matured (Figure 6, E-G). Accordingly, nerve conduction velocity was improved by the increased levels of active Pfn1 (Figure 6H). The most striking effect of S138A hPfn1 delivery after sciatic nerve injury was restoration of mechanical nociception as

it became undistinguishable from uninjured controls, while it was still severely impaired in AAV-GFP expressing animals (Figure 6I). Altogether, our data places constitutively active Pfn1 as an attractive target for therapeutic strategies to induce peripheral nerve regeneration and functional recovery.

To further emphasise the action of active Pfn1 as a pro-regenerative molecule promoting axon regeneration in vivo, AAV-mediated delivery of S138A hPfn1 was conducted using a severe model of CNS trauma, complete spinal cord transection. Two weeks following viral administration through the tail vein (day -14, Figure 6J), injury was performed (day 0, Figure 6J). Six weeks following SCI, GFP expressing axons were traced within the lesion site (Figure 6K and Supplemental Figure 3F). In comparison to animals injected with control AAV-GFP, animals treated with AAVs carrying GFP.P2A.S138A hPfn1 showed a 2.4-fold increased number of GFP^+ axons with the ability of penetrating the glial scar (Figure 6, L and M) that displayed a 1.6-fold increased mean distance of regrowth from the rostral lesion border (Figure 6N). Whereas in control AAV-GFP-injected animals only 3% of the axons regenerated over distances above 450 µm, in GFP.P2A.S138A hPfn1-treated mice nearly 25% of the axons were able to regrow long distances from the rostral lesion border (Figure 6O). These observations support that in vivo delivery of active Pfn1 enhances the ability of regenerating axons to penetrate and grow within the inhibitory glial scar environment, in accordance with in vitro neurite outgrowth experiments in a non-permissive substrate (Figure 4N). Combined, our findings indicate that increasing Pfn1 levels and activity enhance axon regeneration both in high and low-regenerative contexts, and hence identify Pfn1 as a novel therapeutic target to promote axon regeneration upon injury.

Discussion

CNS regeneration is largely abortive in higher vertebrates since the plastic embryonic mechanisms underlying axon growth are not reactivated following injury or disease. Damaged axons must assemble motile growth cones to restore functional deficits after trauma. This is likely dictated by the coordinated interplay between cytoskeleton components (43). The mechanical forces resulting from actin polymerization beneath the protruding membrane of the growth cone assign actin dynamics a fundamental role for growth cone motility, extension rate and direction of axon growth (44). Of note, actin and MT dynamics are intimately associated through crosslinkers, which help guiding MTs towards preferential locations at peripheral growth cone edges (45). Interestingly, early in development, when neuronal symmetry is broken due to local protrusive events against the membrane, Cfl directs neurite formation by controlling actin retrograde dynamics and generating space for MT protrusion (15). Similarly, additional proteins regulating actin dynamics at the growth cone may play important roles for the crosstalk between actin and MTs, thereby strengthening the axon (re)growth potential. Here we identify Pfn1 as one of such proteins. In addition to the actin polymerization promoting activity in growth cones, we show that neuronal Pfn1 profoundly modulates MT dynamics, by supporting accelerated growth rates in axonal tips and by localizing growing MTs to growth cone filopodia. Enhanced non-muscle myosin II-based actin retrograde flow is generally viewed to slow down the rate of growth cone advance (46-48). Here, similarly to (19), we show that in conditions of optimal axon regrowth such as those generated by CL, actin retrograde is increased. Of note, actin retrograde flow can sweep MTs backwards in growth cones (49-51). In contrast, we show that increased actin retrograde flow can occur concomitantly with increased MT protrusion into growth cone filopodia. Interestingly, dynein is capable of enabling MTs to overcome non-muscle myosin II-driven forces allowing their advance into growth cone filopodia, opposing axon retraction (52). Putative molecular players allowing fast MT advance powered by Pfn1 in growth cones, in conditions of increased actin retrograde flow, should be further investigated.

Despite their similarities, Pfn1 and Pfn2 have different binding partners (53). This different ligand specificity can underlie distinctive molecular functions. In fact, Pfn2 hinders neuritogenesis (54), supporting the specific effect of Pfn1 here described. Of note, whereas tubulin can be captured from a brain tissue extract on a Pfn1 column (53), it is absent when using Pfn2 affinity chromatography (53). In fact, our data supports that Pfn1, but probably not Pfn2, is a molecular linker of the actin and MT cytoskeletons. Additional in vitro assays using isolated proteins showed that tubulin and Pfn1 could be co-immunoprecipitated (26). More recently, using TIRF analysis in in vitro systems Pfn1 was shown to bind directly to MTs (25). Here we demonstrate that in the growth cone of cultured primary neurons, Pfn1 interferes both with MT growth speed and with MT invasion of filopodia. Whereas the effect of Pfn1 on MT growth speed is not secured by direct tubulin binding but by a positive cooperation with formins, its effect on localizing MTs to growth cone filopodia requires both direct MT-binding and formins. Formins bind directly to MTs generally through the actin-related FH2 domain (36). Alternatively, formins can also associate with the MT plus-tip protein EB1 and thereby accumulate at MT plus-ends, from where they nucleate and accelerate actin polymerization (55). Given that formins are only capable of potentiating actin elongation in the presence of Pfn, formin-Pfn complexes are probably important players in mediating the communication of the MT and actin cytoskeletons in growth cones. Indeed, peripheral dynamic MTs are deeply influenced by actin movements, as MTs are physically coupled to actin retrograde flow in the vertebrate growth cone periphery and exhibit similar rates of backward transport (56). Pfn1 is therefore perfectly suited to act as a molecular sensor coordinating the distribution of actin and MTs from a finite pool of basic units to distinct cytoskeleton networks.

In summary, we show that Pfn1 acts as a key coordinator of both actin and MT cytoskeletons in growth cones and thereby promotes axon growth and regeneration capacity. Most importantly, we demonstrate that in vivo viral delivery of active Pfn1 promotes axon regeneration and functional recovery of the injured sciatic nerve, and increases axon regeneration through the inhibitory glial scar after spinal cord injury. Our results indicate that modulation of Pfn1 levels and activity is instrumental to successfully produce a positive

regeneration outcome. Of note, AAVs are emerging as very attractive vehicles for clinical gene therapy of human nervous system disorders, given their low immunogenicity and toxicity and the ability of specific serotypes to cross the blood-brain barrier after intravenous delivery (42). In the future, AAV-mediated delivery of constitutively active Pfn1, together with the identification of modulators of Pfn1 activity with therapeutic potential, should be considered for the treatment of the injured nervous system.

Methods

Animals. Pfn1 neuronal-specific conditional knockout mice (cre^{+}Pfn1$^{fl/fl}$), were generated by crossing homozygous floxed Pfn1 mice (Pfn1$^{fl/fl}$ (57)) and Single-neuron Labelling with Inducible Cre-mediated Knockout (SLICK)-H mice (58). SLICK-H co-express tamoxifen-inducible CreER^{T2} recombinase and YFP under the neuronal-specific Thy1 promoter. Cre^{+}Pfn1$^{fl/wt}$ mice were crossed to Pfn1$^{fl/wt}$ mice such that cre^{+}Pfn1$^{fl/fl}$ and cre^{+}Pfn1$^{wt/wt}$ mice were generated. Genotyping was as described (57). Cre recombinase was induced by tamoxifen injection (75mg/kg; Sigma-Aldrich) at weaning during 5 days. Given tamoxifen neuroprotective effects, controls were tamoxifen-treated cre^{+}Pfn1$^{wt/wt}$ mice. Mice of either sex were used in all cre^{+}Pfn1 procedures. For AAV-mediated delivery of hPfn1, C57BL/6 mice (12-15 weeks old) were used; for SCI experiments, only females were utilized whereas both sexes were used for sciatic nerve crush. Experimental conditions were randomized and surgeries were performed blinded to experimental conditions.

Primary cultures. DRG neuron cultures were performed as described (59). DRG from 7-8 weeks old cre^{+}Pfn1 mice or 6-8 weeks old Wistar rats were used. For experiments in which DRG were conditioned, sciatic nerve transection was done 1 week prior culture. Electroporation of DRG neurons was performed with 4D-Nucleofector^{TM} System (mouse DRG neurons: program CM-137; rat DRG neurons: program CM-138) at a cell density of at least 200,000 cells/condition and left in suspension for 24 hr at 37°C in 5% CO_2. Subsequently, cells were grown on 13 mm coverslips (for neurite outgrowth assays) or 8-well µ-dishes (IBIDI-80827, for live imaging assays) coated with poly-L-lysine (20 µg/mL, PLL, Sigma, P2636) and laminin (5 µg/mL, Sigma, L2020) for 12-14 hr until fixing or imaging. For experiments using aggrecan (Sigma-Aldrich, A1960-1MG), DRG neurons were plated in either PLL:laminin (20:5 µg/mL) or PLL:laminin:aggrecan (20:5:20 µg/mL). Culture medium was DMEM:F12 (Sigma, D8437) supplemented with 1x B27 (Gibco), 1% penicillin/streptomycin (Gibco), 2 mM L-glutamine (Gibco) and 50 ng/mL NGF (Millipore, 01-125). Hippocampal neurons were cultured as described (60). Electroporation was performed

at a cell density of at least 750,000 cells/condition (program CU110). Cells were plated either in 13 mm coverslips or 8-well µ-dishes coated with PLL (20 µg/mL) grown in Neurobasal medium supplemented with 1% penicillin-streptomicin, 1× B27, 2 mM L-glutamine, and maintained at 37°C in 5% CO_2. Hippocampal neurons at DIV4 (for axon growth analysis) or DIV7 (for dendritic growth analysis) and DRG neurons (12-14 hr post-plating) were fixed for immunostaining or imaged for live-cell experiments, as detailed below.

Plasmids and viral vectors. The full-length human Pfn1 open reading frame (WT hPfn1, cloned in the pCMV-SPORT6 vector, Addgene, clone IRATp970C034D) and different hPfn1 mutants were used. Specific WT hPfn1 residues were mutated to generate a shRNA-resistant WT hPfn1 (WT hPfn1*), phospho-resistant constitutively active hPfn1 (S138A hPfn1), poly-proline binding-deficient hPfn1 (H134S hPfn1) and MT binding-deficient hPfn1 (G118V hPfn1). Mutants were obtained using the QuickChange II XL kit (Agilent Technologies) and mismatched primers introducing 1 or 2 bp substitutions. Pfn1 (target sequence: CGGTGGTTTGATCAACAAGAA, TRCN0000011969, Sigma) and Pfn2 (target sequence: ACGTTGATGGTGACTGCACAA, TRCN0000071642, Sigma) shRNA constructs were used in hippocampal and DRG neuron cultures and in CAD cells (European Collection of Authenticated Cell Cultures, cat# 08100805) to downregulate Pfn1 and Pfn2 protein levels, respectively. For the in vivo delivery of S138A hPfn1 and H134S/S138A hPfn1, AAVs were used. In detail, GFP linked to S138A hPfn1 by the 2A self-cleaving small peptide P2A, was cloned into an AAV-PHP.eB plasmid to obtain the constructs pAAV-GFP.P2A.S138A hPfn1 and pAAV-GFP.P2A.H134S/S138A hPfn1. Control AAV vectors, where Pfn1 was replaced by a 5 glycine sequence (pAAV-GFP), were also generated. Viral vectors are hereafter referred to as AAV-GFP, AAV-GFP.P2A.S138A hPfn1 or AAV-GFP.P2A.H134S/S138A hPfn1. Expression was driven by the neuronal promoter synapsin. AAV-PHP.eB particles were produced by Vector Builder and enabled neuronal-specific targeting of the nervous system following systemic delivery (42).

Neurite outgrowth and growth cone morphology. Neurite outgrowth was assessed following immunofluorescence against βIII-tubulin. DRG neuron cultures of cre^{+}Pfn1$^{fl/fl}$ and cre^{+}Pfn1$^{wt/wt}$ mice were fixed 12-14 hr post-plating with 4% paraformaldehyde (PFA). Incubation with mouse anti-βIII-tubulin (1:1,000; Promega, G7121) was done overnight at 4°C. The secondary antibody was donkey anti-mouse Alexa Fluor 594 (1:1,000; Jackson ImmunoResearch Labs, 715-585-150). Images were acquired in an epifluorescence Zeiss Axio Imager Z1 microscope with an Axiocam MR3.0 camera and Axiovision 4.7 software. Neurite tracing and branching analyses were performed in Matlab with Synapse Detector software (61) to quantify neurites crossing concentric circles centered at the cell body with radiuses of consecutive multiples of 25 µm. In experiments in which WT hPfn1 or S138A hPfn1 overexpression was performed, dissociated adult rat DRG neurons were electroporated (as detailed above) with a mixture of GFP (0.2 µg, pmaxGFP^{TM}, Lonza) and hPfn1 (0.6 µg) encoding plasmids, plated at a cell density of 7,500 cells/well, fixed 12-14 hr post-plating and stained for βIII-tubulin as described above. Image acquisition was performed using a Leica DMI 6000B with an ORCA-Flash4.0 V2 C11440-22CU digital camera and Leica Application Suite Advanced Fluorescence (LAS AF) software. Experiments using shRNA constructs followed similar procedures. Specifically, mixtures of pmaxGFP^{TM}:shRNA Pfn1 (0.2:1.2 µg) or *Discosoma sp.* red fluorescent protein (DsRed, Clontech):shRNA Pfn2 encoding plasmids (0.5:1.5 µg) were used; control experimental conditions were nucleofected with the empty plasmid pLKO.1 (CTR, Addgene). E18 rat hippocampal neurons were electroporated following the same strategy and fixed at DIV4 or DIV7. For Pfn1 depleted hippocampal neurons, axon and dendrite length were traced manually with NeuronJ plugin for ImageJ. Axonal tracing was also performed in DIV4 hippocampal neurons co-transfected with pmaxGFP^{TM} (0.2 µg) and S138A hPfn1, G118V/S138A hPfn1, or H134S/S138A hPfn1 (0.6 µg). Polarization analysis of hippocampal neurons was assessed as detailed (15). Morphometric evaluation of growth cones was performed in both cre^{+}Pfn1$^{fl/fl}$ and cre^{+}Pfn1$^{wt/wt}$ adult DRG neurons and hippocampal neurons expressing shRNA Pfn2 plasmid. Neurons were stained with mouse anti-βIII-tubulin (1:5,000) overnight at 4°C and

incubated for 1 hr at room temperature with donkey anti-mouse Alexa Fluor 647 (1:500; Jackson ImmunoResearch Labs, 715-605-150) secondary antibody and with rhodamine conjugated phalloidin (1:50; Thermo Fisher Scientific, R415) diluted 1:10 in blocking buffer. Images were acquired by epifluorescence on a Zeiss Axio Imager Z1 microscope with an Axiocam MR3.0 camera and Axiovision 4.7 software. Only growth cones of YFP^+/βIII-tubulin$^+$ (in case of DRG neurons from cre$^+$Pfn1 mice) and GFP^+ neurons (in the case of hippocampal neurons co-nucleofected with pmaxGFP^{TM} (Lonza)) were analysed by measuring the total area of the growth cone, and the filopodia number and size using ImageJ software. To quantify endogenous Pfn1 fluorescence in naïve and conditioned DRG growth cones, neurons were fixed 12-14 hr post-plating with 2% PFA, stained with rabbit anti-Pfn1 (1:400; Abcam, ab50667) overnight at 4°C and incubated for 1 hr at room temperature with donkey anti-mouse Alexa Fluor 594 (1:1,000) and goat anti-rabbit Alexa Fluor 488 (1:1,000; Jackson ImmunoResearch Labs, 111-545-003) secondary antibodies in blocking buffer. Images were acquired by epifluorescence as described above. A line scan across growth cones was drawn, a plot of grey values was done in relation to the distance from the growth cone leading edge and corresponding values were extracted and compared (for each image the highest grey value was considered 100%).

*Live cell imaging***.** For the analysis of actin and MT dynamics in the growth cone, adult DRG neurons from 7-8 weeks old cre$^+$Pfn1$^{fl/fl}$ and cre$^+$Pfn1$^{wt/wt}$ mice were isolated as described and nucleofected with LifeAct-RFP (62) (0.75 µg) or EB3-mcherry (0.5 µg; (63)) encoding plasmids, respectively. Twelve hr after plating, time-lapse recordings were performed in phenol-free DMEM:F12 supplemented as mentioned above, at 37°C and 5% CO_2, on a Spinning Disk Confocal System Andor Revolution XD with an iXonEM+ DU-897 camera and a IQ 1.10.1 software (ANDOR Technology, UK). Only transfected RFP^+/YFP^+ or mcherry$^+$/YFP^+ neurons were considered for analysis. For both the quantification of actin retrograde flow and of EB3 comet growth speed, kymographs were performed using the Fiji KymoResliceWide plugin (distance-x axis; time-y axis). Starting and end positions of the

traces were defined using Fiji Cell Counter plugin. In live imaging experiments using hippocampal or DRG neurons from Wistar rats, plasmids expressing either LifeAct-GFP (0.75 µg) (62) or EB3-GFP (0.5 µg) (64) were co-nucleofected alongside plasmids of interest. Actin retrograde flow and EB3 comet speed were quantified in these neurons, as well as the EB3 comet invasion per filopodia. The invasion frequency of dynamic MTs was quantified by counting the number of EB3 comet invasions (using Fiji plugin Cell Counter) divided by the number of filopodia. A similar approach was used in SMIFH2 (5µM, Sigma, S4826) treated cells. SMIFH2 is a general formin inhibitor that targets diverse formin isoforms (38), decreasing their affinity towards the barbed end of actin filaments, preventing both actin nucleation and processive barbed-end elongation. In SMIFH2 experiments, hippocampal neurons underwent two drug treatments, at DIV3 and at DIV4, 1 hr before fixing.

Immunoblotting. Protein lysates of rat SCI site (collected 2.5 mm rostral and 2.5 mm caudal to the lesion site of animals with either SCI or CL 1 week following injury), DRG, brain (from $cre^{+}Pfn1^{fl/fl}$ and $cre^{+}Pfn1^{wt/wt}$ mice) or CAD cell extracts were prepared in ice-cold lysis buffer containing 0.3% Triton X-100 (Sigma), protease inhibitors (cOmplete, Mini; Roche) and 2 mM orthovanadate, separated under denaturing conditions, transferred to Amersham™ Protran™ Premium 0.45 µm nitrocellulose membranes (GE Healthcare Life Sciences) and probed with primary antibodies (in 5% BSA or 5% milk in TBS-T) overnight at 4°C. Primary antibodies used were: rabbit anti-Pfn1 (either 1:1,000; Thermo Fisher Scientific, PA5-17444 or 1:1,000; Abcam, ab50667), rabbit anti-Pfn1 pS138 (1:1,000, provided by Dr Jieya Shao, University of California, San Francisco, USA), rabbit anti-Pfn2 (1:1,000, provided by Dr Pietro Pilo Boyl, Institute of Genetics University of Bonn, Germany), mouse anti-β-actin (1:5,000; Sigma-Aldrich, A5441), mouse anti-α-tubulin (1:1,000; Sigma-Aldrich, T6199), rabbit anti-HPRT (1:1,000; Santa Cruz Biotechnology, sc-20975), rabbit anti-ROCK1 (1:1,000, Abcam, ab134181, clone EPR638Y) and rabbit anti-vinculin (1:1,000; Abcam, ab129002). Secondary antibodies were used in 5% non-fat dried milk in TBS-T for 1 hr at room temperature: donkey anti-mouse IgG conjugated with horseradish peroxidase (HRP)

(1:5,000; Jackson ImmunoResearch Labs, 715-035-151) and donkey anti-rabbit IgG conjugated with HRP (1:5,000; Jackson ImmunoResearch Labs, 711-035-152). Membranes were incubated with Luminata Crescendo Western HRP substrate (Millipore), exposed to Fuji Medical X-Ray Film (Fujifilm), scanned on a Molecular Imager GS800, and quantified using Quantity One 1-D Analysis Software version 4.6 (Bio-Rad).

Analysis of peripheral axon regeneration and functional recovery. Adult 12 weeks old mice were deeply anesthetised with isoflurane. Sciatic nerves were crushed at the mid-thigh level for 15 s two consecutive times using a hemostatic forcep (13010-12, FST) producing a well-defined lesion area. For histological analysis of axon regeneration, remyelination and NMJ establishment in cre^{+}Pfn1 mice, animals were sacrificed at 7, 15 or 28 days post-injury. To analyse regenerated myelinated sciatic nerve axons and g-ratio, nerves were collected at the same anatomical position distal to the crush site, just above the bifurcation of the sciatic nerve, fixed in 4% glutaraldehyde in 0.1 M cacodylate buffer (pH 7.4) for 1 week, post-fixed with 1% OsO_4 in 0.1 M sodium cacodylate buffer (pH 7.4) for 2 hr and dehydrated and embedded in Epon (Electron Microscopy Sciences). Sections (1 µm thickness) were stained for 10 min with 1% p-phenylenediamine (PPD) in absolute methanol, dried, and mounted on DPX (Merk). Images of the lesion area were acquired using an Olympus optical microscope with an Olympus DP 25 camera and analysed in Photoshop (Adobe). The total number of myelinated axons was determined in each cross section and divided by its area. Analysis of unmyelinated axons was not performed in cre^{+}Pfn1 mice, as cre expression only occurs in a small percentage of small unmyelinated neurons. The *g*-ratio was calculated by dividing the diameter of each axon by its myelin-including diameter in over 50 axons per animal. For the morphometric evaluation of NMJs, the lateral gastrocnemius was dissected in PBS under a stereomicroscope, and fixed for 24 hr with 4% PFA at 4°C. Isolated muscles were permeabilized for 30 min with 1% Triton X-100 at room temperature, and the autofluorescence quenched with 0.2M NH_4Cl (Merck) and 0.1% sodium borohydride (Sigma). After 1 hr blocking (1mg/ml BSA, 0.2% Triton X-100), tissues were incubated 1 hr with BTX

conjugated-rhodamine (1:250, ThermoFischer Scientific, T1175) in blocking buffer at room temperature. NMJ morphometric analysis was carried out in Z-stack of images taken in a Leica TCS SP8 microscope, 3D-rendered using the Huygens Professional software (Scientific Volume Imaging, SVI) and analysed for volume. Analysis of motor nerve conduction velocity was performed as described (65) with a PowerLab 4/25T (AD Instruments) using Chart5 software. Conduction velocities were calculated as (proximal distance−distal distance)/(proximal latency − distal latency). To assess regeneration of sciatic nerve axons following AAV-PHP.eB-mediated delivery of S138A hPfn1 or H134S/S138A hPfn1, the sciatic nerve was crushed 2 weeks after systemically injecting AAV-GFP, AAV-GFP.P2A.S138A hPfn1 or AAV-GFP.P2A.H134S/S138A hPfn1 ($6e^{11}$vg/mouse) through the tail vein, using the AAV-PHP.eB capsid that allows non-invasive gene delivery to the nervous system (42). Mice recovered for 3 or 28 days before sacrifice. Nerves were collected after 4% PFA perfusion, post-fixed for 3 days at 4°C, and cryoprotected in 30% sucrose. Tissues were embedded in optimum cutting temperature compound (Thermo Fisher Scientific), frozen and sectioned longitudinally (Leica) at 15 µm thickness. In these nerves, SCG10 expression was detected by immunofluorescence using a rabbit anti-SCG10/Stathmin-2 (1:10,000; Novus, NBP1-49461). Image acquisition was performed using In Cell Analyzer 2000 (GE Healthcare) and analysed using Fiji software. Quantification of SCG10 fluorescence was performed in longitudinal sections by scanning a thickness similar to that of the nerve sample. A plot of mean grey values was done in relation to the distance of the lesion epicentre. Axon regeneration was additionally quantified distally to the injury site by measuring the distance from the distal tip of GFP^+ regenerating axons to the lesion border (up to 4 sections per animal were analysed). Data represents the mean distance for each condition, considering all regenerating axons. Accumulation of nuclei of inflammatory cells within the crush site was visualized after DAPI counterstaining and used to define the lesion area. Regenerating axons were seen as continuous structures that could be clearly separated from degenerating swollen axonal fragments under high magnification. Analysis of NMJs and motor nerve conduction velocity was conducted as described above.

For Von Frey Hair testing, animals were acclimatized for 20 min in a chamber with a wire mesh bottom allowing access to hind paws. Retractable monofilaments (Aesthesio®, Precise Tactile Sensory Evaluator, 37450-275) were used to apply a force to the mid-plantar surface on hind paws. Clear paw withdrawal or abrupt moving were considered positive responses. Withdrawal threshold equaled the weakest force to elicit paw withdrawal on ≥ 50% of the trials (n=5 trials). The percentage of the withdrawal threshold shown is an averaged value of right and left hind paws relative to baseline recordings done in uninjured AAV-GFP-injected animals.

Analysis of axon regeneration following spinal cord injury. Adult 8 weeks old cre^{+}Pfn1 mice and 15 weeks old female C57BL/6 mice were deeply anesthetised with isoflurane. Laminectomy was performed at the thoracic T8-T9 level and the spinal cord was cut using a micro feather ophthalmic scalpel (Feather, Safety Razor Co). For CL experiments, animals were subjected to a sciatic nerve transection 1 week prior SCI. In cre^{+}Pfn1 mice, analysis of dorsal column axon regeneration after either SCI or CL was performed 4 weeks post-injury. Dorsal column axons were traced by injecting 2 µl of 1% CT-B (List Biologicals, 103B) with a 10 µl syringe (Hamilton, USA) into the left sciatic nerve 4 days prior euthanasia (day 24 PI). On day 28, mice were perfused with 4% PFA and the spinal cords were post-fixed for 1 week at 4°C and later cryoprotected in 30% sucrose. Serial tissue sagittal cryosections (50 µm thickness) were collected for free floating immunohistochemistry. Sections were incubated overnight at 4ºC with goat anti-CT-B primary antibody (1:30,000; List Biologicals, 703). Antigen detection was amplified by incubating samples with biotinylated horse anti-goat (1:200; Vector) for 2 hr at room temperature and subsequently with Alexa Fluor 568 streptavidin (1:1,000, Invitrogen) for 1 hr at room temperature. Dorsal column fiber images were acquired by confocal microscopy on a Leica TCS SP5 II with LAS AF software and analysed using Fiji software. Regeneration of dorsal column axons was quantified by measuring the distance from the rostral tip of all regenerating YFP^{+}/CT-B^{+} axons to a vertical

line placed at the rostral end of the dorsal column tract (up to 6 sections per animal). Data presented is the mean distance for each condition, considering all regenerating axons.

To assess axon regeneration of spinal cord axons following AAV-PHP.eB-mediated delivery of Pfn1, spinal cord transection was performed 2 weeks after systemically injecting AAV-GFP, AAV-GFP.P2A.S138A hPfn1 or AAV-GFP.P2A.H134S/S138A hPfn1 ($4e^{11}$vg/mouse) through the tail vein, using the AAV-PHP.eB capsid that allows non-invasive gene delivery to the nervous system (42). Injured spinal cord tissue was collected 6 weeks after SCI and processed as aforementioned; image acquisition was performed using the IN Cell Analyzer 2000 microscope (GE Healthcare) and analysed using Fiji software. The total number of GFP^+ axons within the glial scar were counted in up to 12 sections per animal. Regenerating rostral to caudal distances were measured from the tip of GFP^+ axons to a vertical line placed perpendicularly to the sagittal axis of the spinal cord at the rostral border of the lesion. Regenerating distances are presented as the mean value considering all regenerating GFP^+ axons, and as a percentage of GFP^+ axons found within different growth distance windows (0-150 μm; 150-300 μm; 300-450 and >450 μm).

Statistics. All statistical tests were performed with GraphPad Prism 6. Unless otherwise stated, the following statistical tests were used: two-tailed Student's t-test, one-way ANOVA with Tukey's post-test, two-way ANOVA with Sidak's and Tukey's post-test. A P value less than 0.05 was considered significant. Statistical tests and sample sizes are indicated in figure legends and significance was defined as * or $^{\#}P < 0.05$, ** or $^{\#\#}P < 0.01$, ***$P < 0.001$, **** or $^{\#\#\#\#}P < 0.0001$, ns or $^{\#}$ns: not significant.

Study approval. Experiments were carried out in accordance with the European Union Directive 2010/63/EU and national Decreto-lei nº113-2013. The protocols described were approved by the IBMC Ethical Committee and by the Portuguese Veterinarian Board.

Author Contributions

MS coordinated the research; MS and RPC designed and analysed the experiments, and wrote the paper; RPC, SCS, SCL, JNR, TFS, DM, JM, ACC, PB and MMS performed the experiments and quantifications; MAL and FB provided conceptual and experimental support; MC and RF provided $Pfn1^{fl/fl}$ mice; FB, MAL, PB and RF critically revised the manuscript.

Acknowledgments

The authors are indebted to Dr F. Mar, R. Baeta and D. Silva (Nerve Regeneration group) for experimental support. We thank the i3S Animal, Cell Culture, Genotyping, Histology and Electron Microscopy, Advanced Light Microscopy and BioSciences Screening (PPBI-POCI-01-0145-FEDER-022122) Facilities. We thank Prof Marco Rust (Philipps-Universität Marburg, Germany) for transferring $Pfn1^{fl/fl}$ mice. Funding was from the International Foundation for Research in Paraplegia (P140), RESOLVE (NORTE-01-0246-FEDER-000018), the Morton Cure Paralyis Fund- MCPF, The Bluepharma | University of Coimbra Innovation Award, and Fundação para a Ciência e a Tecnologia (FCT)/Ministério da Ciência, Tecnologia e Ensino Superior (NORTE-01-0145-FEDER-028623). RPC, SCS, JNR and ACC are FCT fellows (SFRH/BD/112112/2015, SFRH/BD/136760/2018, SFRH/BD/131565/2017 and SFRH/BD/143926/2019, respectively). ML is a FCT Investigator.

References

1. Mar FM, Bonni A, and Sousa MM. Cell intrinsic control of axon regeneration. *EMBO Rep.* 2014;15(3):254-263.
2. Nascimento AI, Mar FM, and Sousa MM. The intriguing nature of dorsal root ganglion neurons: Linking structure with polarity and function. *Prog Neurobiol.* 2018;168:86-103.
3. Neumann S, and Woolf CJ. Regeneration of dorsal column fibers into and beyond the lesion site following adult spinal cord injury. *Neuron.* 1999;23(1):83-91.
4. Blanquie O, and Bradke F. Cytoskeleton dynamics in axon regeneration. *Curr Opin Neurobiol.* 2018;51:60-69.
5. Gomez TM, and Letourneau PC. Actin dynamics in growth cone motility and navigation. *J Neurochem.* 2014;129(2):221-234.
6. Bradke F, and Dotti CG. The role of local actin instability in axon formation. *Science.* 1999;283(5409):1931-1934.
7. Lowery LA, and Van Vactor D. The trip of the tip: understanding the growth cone machinery. *Nat Rev Mol Cell Biol.* 2009;10(5):332-343.
8. Joset A, Dodd DA, Halegoua S, and Schwab ME. Pincher-generated Nogo-A endosomes mediate growth cone collapse and retrograde signaling. *Journal of Cell Biology.* 2010;188(2):271-285.
9. Mimura F, Yamagishi S, Arimura N, Fujitani M, Kubo T, Kaibuchi K, et al. Myelin-associated glycoprotein inhibits microtubule assembly by a rho-kinase-dependent mechanism. *Journal of Biological Chemistry.* 2006;281(23):15970-15979.
10. Monnier PP, Sierra A, Schwab JM, Henke-Fahle S, and Mueller BK. The Rho/ROCK pathway mediates neurite growth-inhibitory activity associated with the chondroitin sulfate proteoglycans of the CNS glial scar. *Mol Cell Neurosci.* 2003;22(3):319-330.
11. Dergham P, Ellezam B, Essagian C, Avedissian H, Lubell WD, and McKerracher L. Rho signaling pathway targeted to promote spinal cord repair. *Journal of Neuroscience.* 2002;22(15):6570-6577.
12. Lehmann M, Fournier A, Selles-Navarro I, Dergham P, Sebok A, Leclerc N, et al. Inactivation of Rho signaling pathway promotes CNS axon regeneration. *Journal of Neuroscience.* 1999;19(17):7537-7547.
13. Fehlings MG, Theodore N, Harrop J, Maurais G, Kuntz C, Shaffrey CI, et al. Phase I/IIa Clinical Trial of a Recombinant Rho Protein Antagonist in Acute Spinal Cord Injury. *J Neurotraum.* 2011;28(5):787-796.
14. Pavlov D, Muhlrad A, Cooper J, Wear M, and Reisler E. Actin filament severing by cofilin. *J Mol Biol.* 2007;365(5):1350-1358.

15. Flynn KC, Hellal F, Neukirchen D, Jacob S, Tahirovic S, Dupraz S, et al. ADF/cofilin-mediated actin retrograde flow directs neurite formation in the developing brain. *Neuron.* 2012;76(6):1091-1107.
16. Didry D, Carlier MF, and Pantaloni D. Synergy between actin depolymerizing factor/cofilin and profilin in increasing actin filament turnover. *J Biol Chem.* 1998;273(40):25602-25611.
17. Garvalov BK, Flynn KC, Neukirchen D, Meyn L, Teusch N, Wu X, et al. Cdc42 regulates cofilin during the establishment of neuronal polarity. *J Neurosci.* 2007;27(48):13117-13129.
18. Wen Z, Han L, Bamburg JR, Shim S, Ming GL, and Zheng JQ. BMP gradients steer nerve growth cones by a balancing act of LIM kinase and Slingshot phosphatase on ADF/cofilin. *J Cell Biol.* 2007;178(1):107-119.
19. Tedeschi A, Dupraz S, Curcio M, Laskowski CJ, Schaffran B, Flynn KC, et al. ADF/Cofilin-Mediated Actin Turnover Promotes Axon Regeneration in the Adult CNS. *Neuron.* 2019;103(6):1073-1085 e1076.
20. Witke W. The role of profilin complexes in cell motility and other cellular processes. *Trends Cell Biol.* 2004;14(8):461-469.
21. Ferron F, Rebowski G, Lee SH, and Dominguez R. Structural basis for the recruitment of profilin-actin complexes during filament elongation by Ena/VASP. *EMBO J.* 2007;26(21):4597-4606.
22. Paul AS, and Pollard TD. Review of the mechanism of processive actin filament elongation by formins. *Cell Motil Cytoskeleton.* 2009;66(8):606-617.
23. Michaelsen-Preusse K, Zessin S, Grigoryan G, Scharkowski F, Feuge J, Remus A, et al. Neuronal profilins in health and disease: Relevance for spine plasticity and Fragile X syndrome. *Proc Natl Acad Sci U S A.* 2016;113(12):3365-3370.
24. Bender M, Stritt S, Nurden P, van Eeuwijk JM, Zieger B, Kentouche K, et al. Megakaryocyte-specific Profilin1-deficiency alters microtubule stability and causes a Wiskott-Aldrich syndrome-like platelet defect. *Nat Commun.* 2014;5:4746.
25. Henty-Ridilla JL, Juanes MA, and Goode BL. Profilin Directly Promotes Microtubule Growth through Residues Mutated in Amyotrophic Lateral Sclerosis. *Curr Biol.* 2017;27(22):3535-3543 e3534.
26. Nejedla M, Sadi S, Sulimenko V, de Almeida FN, Blom H, Draber P, et al. Profilin connects actin assembly with microtubule dynamics. *Mol Biol Cell.* 2016;27(15):2381-2393.
27. Metzler WJ, Bell AJ, Ernst E, Lavoie TB, and Mueller L. Identification of the poly-L-proline-binding site on human profilin. *J Biol Chem.* 1994;269(6):4620-4625.

28. Lassing I, and Lindberg U. Specific interaction between phosphatidylinositol 4,5-bisphosphate and profilactin. *Nature.* 1985;314(6010):472-474.
29. Smith DS, and Skene JH. A transcription-dependent switch controls competence of adult neurons for distinct modes of axon growth. *J Neurosci.* 1997;17(2):646-658.
30. Shin JE, Geisler S, and DiAntonio A. Dynamic regulation of SCG10 in regenerating axons after injury. *Exp Neurol.* 2014;252:1-11.
31. Shao J, Welch WJ, Diprospero NA, and Diamond MI. Phosphorylation of profilin by ROCK1 regulates polyglutamine aggregation. *Mol Cell Biol.* 2008;28(17):5196-5208.
32. Fujita Y, and Yamashita T. Axon growth inhibition by RhoA/ROCK in the central nervous system. *Front Neurosci.* 2014;8:338.
33. Wu CH, Fallini C, Ticozzi N, Keagle PJ, Sapp PC, Piotrowska K, et al. Mutations in the profilin 1 gene cause familial amyotrophic lateral sclerosis. *Nature.* 2012;488(7412):499-503.
34. Kovar DR, Harris ES, Mahaffy R, Higgs HN, and Pollard TD. Control of the assembly of ATP- and ADP-actin by formins and profilin. *Cell.* 2006;124(2):423-435.
35. Kovar DR, Kuhn JR, Tichy AL, and Pollard TD. The fission yeast cytokinesis formin Cdc12p is a barbed end actin filament capping protein gated by profilin. *J Cell Biol.* 2003;161(5):875-887.
36. Bartolini F, Moseley JB, Schmoranzer J, Cassimeris L, Goode BL, and Gundersen GG. The formin mDia2 stabilizes microtubules independently of its actin nucleation activity. *J Cell Biol.* 2008;181(3):523-536.
37. Chesarone MA, DuPage AG, and Goode BL. Unleashing formins to remodel the actin and microtubule cytoskeletons. *Nat Rev Mol Cell Biol.* 2010;11(1):62-74.
38. Rizvi SA, Neidt EM, Cui J, Feiger Z, Skau CT, Gardel ML, et al. Identification and characterization of a small molecule inhibitor of formin-mediated actin assembly. *Chem Biol.* 2009;16(11):1158-1168.
39. Dent EW, Gupton SL, and Gertler FB. The growth cone cytoskeleton in axon outgrowth and guidance. *Cold Spring Harb Perspect Biol.* 2011;3(3).
40. Prokop A, Beaven R, Qu Y, and Sanchez-Soriano N. Using fly genetics to dissect the cytoskeletal machinery of neurons during axonal growth and maintenance. *Journal of Cell Science.* 2013;126(11):2331-2341.
41. Qu Y, Hahn I, Lees M, Parkin J, Voelzmann A, Dorey K, et al. Efa6 protects axons and regulates their growth and branching by inhibiting microtubule polymerisation at the cortex. *Elife.* 2019;8.
42. Chan KY, Jang MJ, Yoo BB, Greenbaum A, Ravi N, Wu WL, et al. Engineered AAVs for efficient noninvasive gene delivery to the central and peripheral nervous systems. *Nat Neurosci.* 2017;20(8):1172-1179.

43. Coles CH, and Bradke F. Coordinating neuronal actin-microtubule dynamics. *Curr Biol.* 2015;25(15):R677-691.
44. Lee CW, Vitriol EA, Shim S, Wise AL, Velayutham RP, and Zheng JQ. Dynamic localization of G-actin during membrane protrusion in neuronal motility. *Curr Biol.* 2013;23(12):1046-1056.
45. Dent EW, and Gertler FB. Cytoskeletal dynamics and transport in growth cone motility and axon guidance. *Neuron.* 2003;40(2):209-227.
46. Lin CH, and Forscher P. Growth Cone Advance Is Inversely Proportional to Retrograde F-Actin Flow. *Neuron.* 1995;14(4):763-771.
47. Toriyama M, Shimada T, Kamiguchi H, Sugiura T, Watanabe N, and Inagaki N. Shootin1 interacts with actin retrograde flow and L1-CAM to promote axon outgrowth. *Neurosci Res.* 2009;65:S45-S45.
48. Nichol RH, Hagen KM, Lumbard DC, Dent EW, and Gomez TM. Guidance of Axons by Local Coupling of Retrograde Flow to Point Contact Adhesions. *Journal of Neuroscience.* 2016;36(7):2267-2282.
49. Schaefer AW, Kabir N, and Forscher P. Filopodia and actin arcs guide the assembly and transport of two populations of microtubules with unique dynamic parameters in neuronal growth cones. *Journal of Cell Biology.* 2002;158(1):139-152.
50. Lin CH, Espreafico EM, Mooseker MS, and Forscher P. Myosin drives retrograde F-actin flow in neuronal growth cones. *Biol Bull-Us.* 1997;192(1):183-185.
51. Yvon AM, Gross DJ, and Wadsworth P. Antagonistic forces generated by myosin II and cytoplasmic dynein regulate microtubule turnover, movement, and organization in interphase cells. *Proc Natl Acad Sci U S A.* 2001;98(15):8656-8661.
52. Myers KA, Tint I, Nadar CV, He Y, Black MM, and Baas PW. Antagonistic forces generated by cytoplasmic dynein and myosin-II during growth cone turning and axonal retraction. *Traffic.* 2006;7(10):1333-1351.
53. Witke W, Podtelejnikov AV, Di Nardo A, Sutherland JD, Gurniak CB, Dotti C, et al. In mouse brain profilin I and profilin II associate with regulators of the endocytic pathway and actin assembly. *EMBO J.* 1998;17(4):967-976.
54. Da Silva JS, Medina M, Zuliani C, Di Nardo A, Witke W, and Dotti CG. RhoA/ROCK regulation of neuritogenesis via profilin IIa-mediated control of actin stability. *J Cell Biol.* 2003;162(7):1267-1279.
55. Henty-Ridilla JL, Rankova A, Eskin JA, Kenny K, and Goode BL. Accelerated actin filament polymerization from microtubule plus ends. *Science.* 2016;352(6288):1004-1009.

56. Marx A, Godinez WJ, Tsimashchuk V, Bankhead P, Rohr K, and Engel U. Xenopus cytoplasmic linker-associated protein 1 (XCLASP1) promotes axon elongation and advance of pioneer microtubules. *Mol Biol Cell.* 2013;24(10):1544-1558.
57. Bottcher RT, Wiesner S, Braun A, Wimmer R, Berna A, Elad N, et al. Profilin 1 is required for abscission during late cytokinesis of chondrocytes. *EMBO J.* 2009;28(8):1157-1169.
58. Young P, Qiu L, Wang D, Zhao S, Gross J, and Feng G. Single-neuron labeling with inducible Cre-mediated knockout in transgenic mice. *Nat Neurosci.* 2008;11(6):721-728.
59. Leite SC, Sampaio P, Sousa VF, Nogueira-Rodrigues J, Pinto-Costa R, Peters LL, et al. The Actin-Binding Protein alpha-Adducin Is Required for Maintaining Axon Diameter. *Cell Rep.* 2016;15(3):490-498.
60. Kaech S, and Banker G. Culturing hippocampal neurons. *Nature protocols.* 2006;1(5):2406-2415.
61. Schmitz SK, Hjorth JJ, Joemai RM, Wijntjes R, Eijgenraam S, de Bruijn P, et al. Automated analysis of neuronal morphology, synapse number and synaptic recruitment. *J Neurosci Methods.* 2011;195(2):185-193.
62. Riedl J, Crevenna AH, Kessenbrock K, Yu JH, Neukirchen D, Bista M, et al. Lifeact: a versatile marker to visualize F-actin. *Nat Methods.* 2008;5(7):605-607.
63. Efimov A, Schiefermeier N, Grigoriev I, Ohi R, Brown MC, Turner CE, et al. Paxillin-dependent stimulation of microtubule catastrophes at focal adhesion sites. *J Cell Sci.* 2008;121(Pt 2):196-204.
64. Stepanova T, Slemmer J, Hoogenraad CC, Lansbergen G, Dortland B, De Zeeuw CI, et al. Visualization of microtubule growth in cultured neurons via the use of EB3-GFP (end-binding protein 3-green fluorescent protein). *J Neurosci.* 2003;23(7):2655-2664.
65. da Silva TF, Eira J, Lopes AT, Malheiro AR, Sousa V, Luoma A, et al. Peripheral nervous system plasmalogens regulate Schwann cell differentiation and myelination. *J Clin Invest.* 2014;124(6):2560-2570.
66. Jockusch BM, Murk K, and Rothkegel M. The profile of profilins. *Rev Physiol Biochem Pharmacol.* 2007;159:131-149.

Figures and Figure Legends

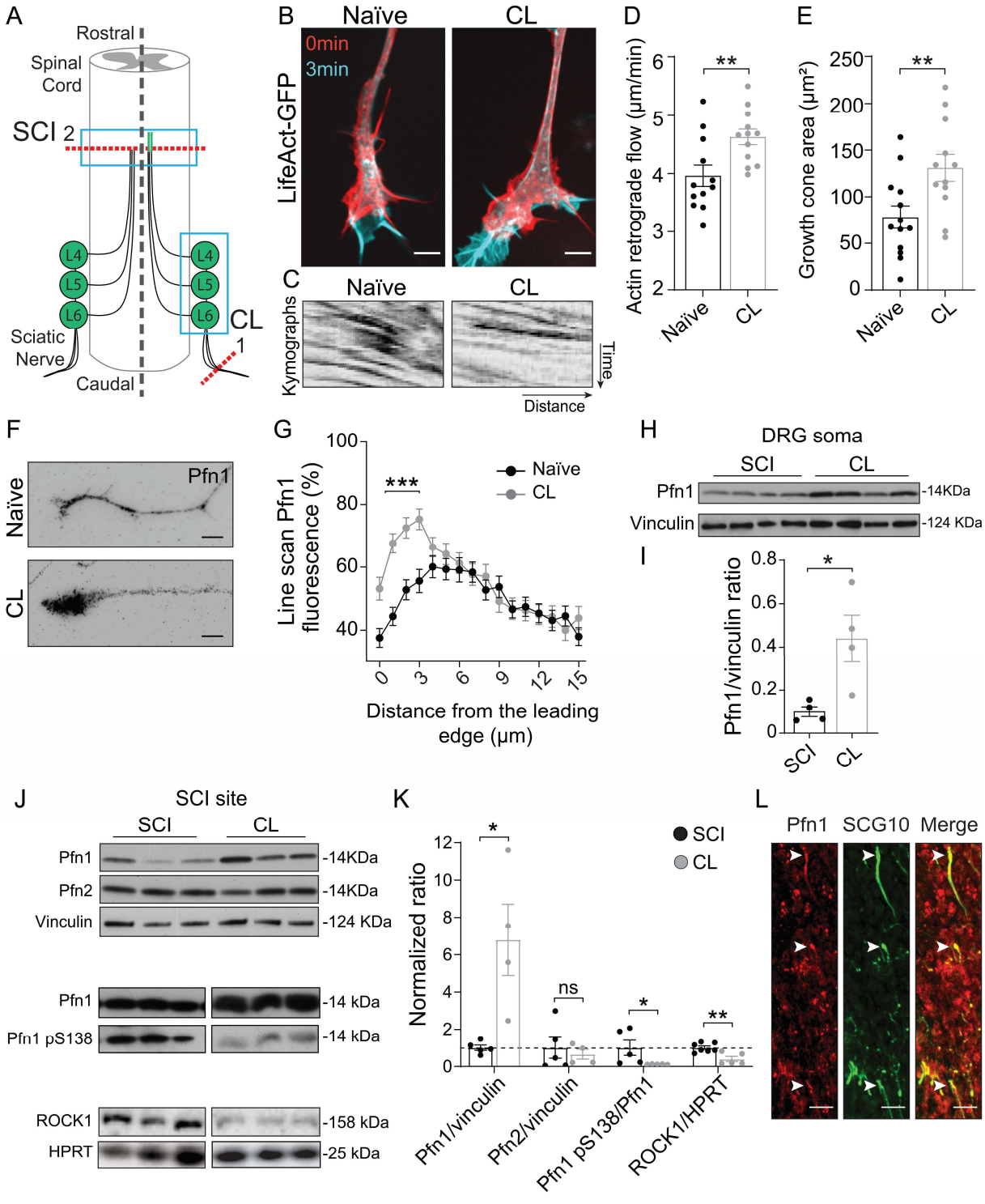

Figure 1. Active Pfn1 is increased after conditioning lesion (CL). (**A**) Representation of SCI and of the CL paradigm (left and right to dashed line, respectively). In CL, a sciatic nerve injury (1) is performed one week prior SCI (2), potentiating regeneration of central DRG axons (right green line, rostral to SCI). WB analyses of the dorsal SCI site and of DRG (blue rectangles) were performed. (**B**) Live-cell imaging of LifeAct-GFP in growth cones of naïve and conditioned adult DRG neurons. Scale bar: 4 µm. (**C**) Kymographs related to (B). (**D**) Quantification of actin retrograde flow and (**E**) growth cone area related to (B). Data represent mean ± SEM (**P < 0.01, t-test, *n* = 12-13 growth cones/condition). (**F**) Pfn1

staining in growth cones of cultured naïve and conditioned DRG neurons. Scale bar: 5 µm. (**G**) Quantification of line scans of Pfn1 fluorescence in relation to distance from growth cone leading edge related to (F). Data represent mean ± SEM (***P < 0.001, two-way ANOVA Sidak's posttest, *n* = 48-57 neurons/condition). (**H**) Western blot and (**I**) respective quantification showing Pfn1 levels in DRG of rats with SCI or CL. Vinculin was used as control. Data represent mean ± SEM (*P < 0.05, t-test, n = 4 animals/condition). (**J**) Western blot and (**K**) respective quantification showing Pfn1, Pfn1 pS138, ROCK1 and Pfn2 levels in samples from the dorsal SCI site (horizontal blue rectangle in (A)), one week after SCI or CL. HPRT and vinculin were used as controls. Data represent mean ± SEM (*P < 0.05, **P < 0.01, ns: not significant, t-test, *n* = 4-7 animals/condition). (**L**) Pfn1 immunofluorescence (red) in sensory SCG10-positive axons (green) in a CL spinal cord. Arrowheads highlight growth cones. Scale bar: 20 µm.

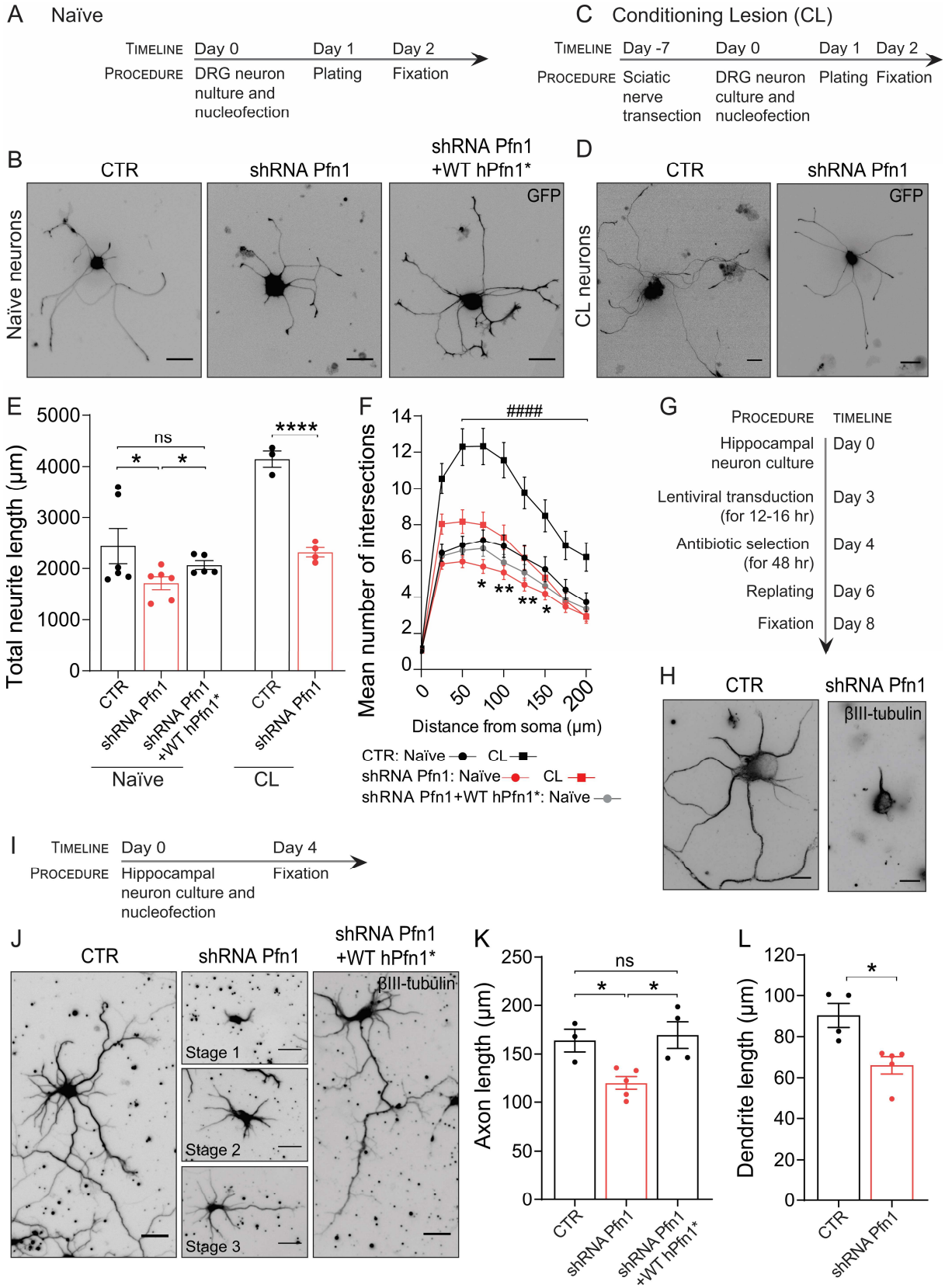

Figure 2. Pfn1 downregulation impairs axon growth in vitro in different neuron types and developmental stages. (A) Timeline of naïve DRG neuron cultures. (**B**) GFP-expressing naïve adult DRG neurons transfected with control empty (CTR) or shRNA Pfn1 plasmid. (**C**) Timeline of conditioned DRG neuron cultures. (**D**) GFP-expressing conditioned

DRG neurons transfected with CTR or shRNA Pfn1 plasmid. Scale bars in (B) and (D): 70 µm. (**E**) Total neurite length related to (B) and (D). Data represent mean ± SEM (*P < 0.05, ****P < 0.0001, ns: not significant, *n* = 3-6 independent samples/condition; 6-36 neurons/sample). (**F**) Branching analysis related to (E). Data represent mean ± SEM (*P < 0.05 and **P < 0.01 refers to CTR versus shRNA Pfn1 of naïve DRG neurons, ####P < 0.0001 refers to CTR versus shRNA Pfn1 of CL DRG neurons, two-way ANOVA Tukey's posttest. (**G**) Timeline for Pfn1 downregulation in DIV3 hippocampal neurons using lentiviral infection. (**H**) βIII-tubulin in hippocampal neurons after lentiviral expression of control empty (CTR) or shRNA Pfn1 plasmid. Scale bar: 10 µm. (**I**) Timeline for Pfn1 downregulation in DIV0 hippocampal neurons. (**J**) βIII-tubulin in DIV4 hippocampal neurons expressing a control empty (CTR) or a shRNA Pfn1 plasmid. Middle panels (shRNA Pfn1) show representative images of stage 1-3 hippocampal neurons; CTR and shRNA Pfn1 +WT hPfn1* scale bar: 30 µm; shRNA Pfn1 scale bar: 20 µm. (**K**) Axon length related to (J). Data represent mean ± SEM (*P < 0.05, ns: not significant, one-way ANOVA Tukey's posttest, *n* = 3-5 independent samples/condition; 11-26 neurons/sample). (**L**) Dendrite length of DIV7 hippocampal neurons expressing control empty (CTR) or shRNA Pfn1 plasmid. Data represent mean ± SEM (*P < 0.05, t-test, *n* = 4-5 independent samples/condition; 3-25 neurons/sample). All rescue experiments were performed using shRNA-resistant WT Pfn1 (WT hPfn1*).

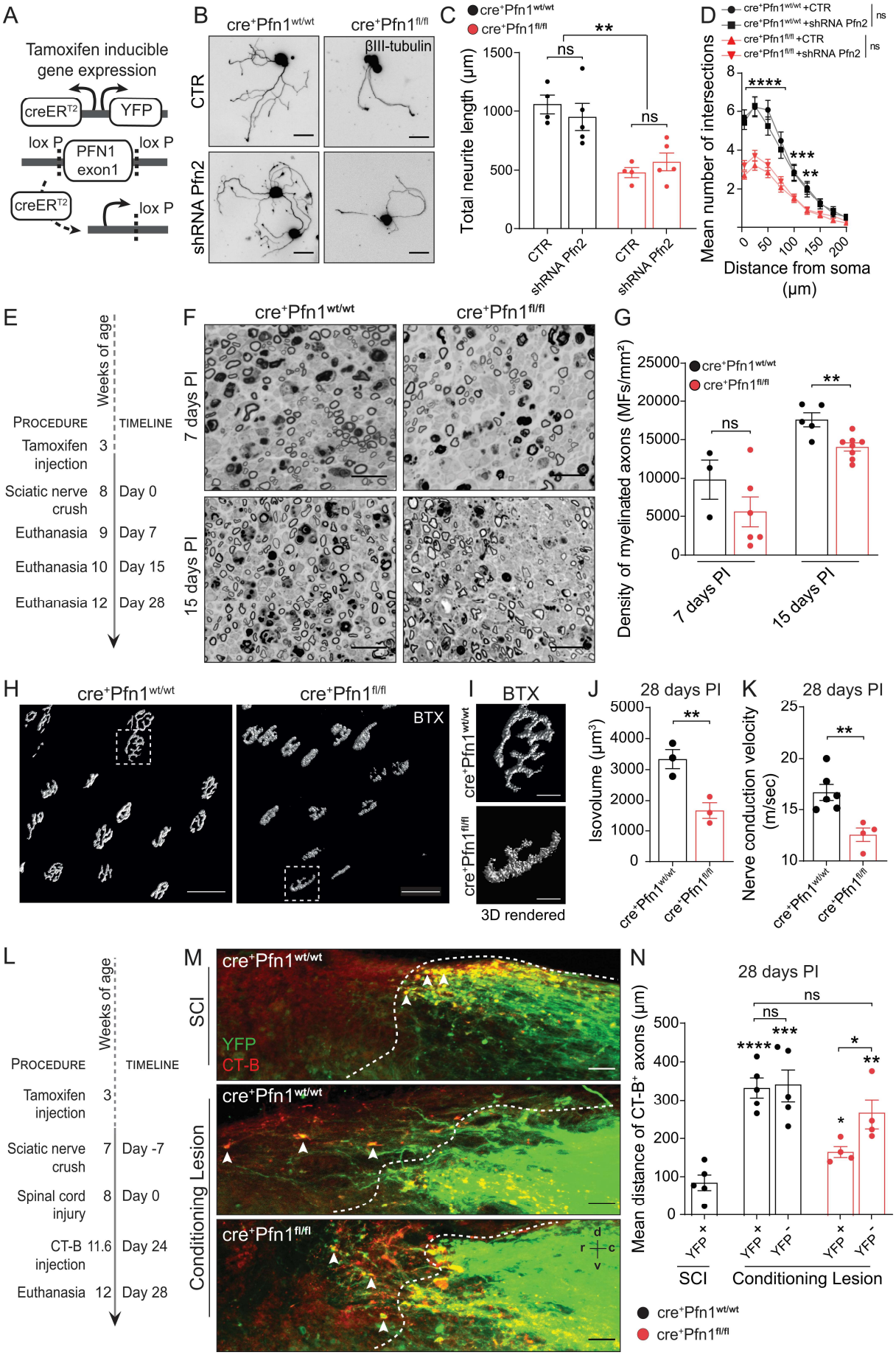
A
Tamoxifen inducible gene expression
creER^{T2}
YFP
lox P
PFN1 exon1
lox P
creER^{T2}
lox P
B
cre^{+}Pfn1$^{wt/wt}$
cre^{+}Pfn1$^{fl/fl}$
βIII-tubulin
CTR
shRNA Pfn2
C
cre^{+}Pfn1$^{wt/wt}$
cre^{+}Pfn1$^{fl/fl}$
Total neurite length (µm)
1500
1000
500
0
**
ns
ns
CTR
shRNA Pfn2
CTR
shRNA Pfn2
D
cre^{+}Pfn1$^{wt/wt}$ +CTR
cre^{+}Pfn1$^{wt/wt}$ +shRNA Pfn2
cre^{+}Pfn1$^{fl/fl}$ +CTR
cre^{+}Pfn1$^{fl/fl}$ +shRNA Pfn2
ns
ns
Mean number of intersections
8
6
4
2
****
***
**
0
50
100
150
200
Distance from soma (µm)
E
Weeks of age
PROCEDURE
TIMELINE
Tamoxifen injection 3
Sciatic nerve crush 8 Day 0
Euthanasia 9 Day 7
Euthanasia 10 Day 15
Euthanasia 12 Day 28
F
cre^{+}Pfn1$^{wt/wt}$
cre^{+}Pfn1$^{fl/fl}$
7 days PI
15 days PI
G
cre^{+}Pfn1$^{wt/wt}$
cre^{+}Pfn1$^{fl/fl}$
Density of myelinated axons (MFs/mm²)
25000
20000
15000
10000
5000
0
ns
**
7 days PI
15 days PI
H
cre^{+}Pfn1$^{wt/wt}$
cre^{+}Pfn1$^{fl/fl}$
BTX
I
BTX
cre^{+}Pfn1$^{wt/wt}$
cre^{+}Pfn1$^{fl/fl}$
3D rendered
J
28 days PI
Isovolume (µm³)
5000
4000
3000
2000
1000
0
**
cre^{+}Pfn1$^{wt/wt}$
cre^{+}Pfn1$^{fl/fl}$
K
28 days PI
Nerve conduction velocity (m/sec)
25
20
15
10
**
cre^{+}Pfn1$^{wt/wt}$
cre^{+}Pfn1$^{fl/fl}$
L
Weeks of age
PROCEDURE
TIMELINE
Tamoxifen injection 3
Sciatic nerve crush 7 Day -7
Spinal cord injury 8 Day 0
CT-B injection 11.6 Day 24
Euthanasia 12 Day 28
M
SCI
Conditioning Lesion
cre^{+}Pfn1$^{wt/wt}$
YFP
CT-B
cre^{+}Pfn1$^{wt/wt}$
cre^{+}Pfn1$^{fl/fl}$
d
r
c
v
N
28 days PI
Mean distance of CT-B^{+} axons (µm)
500
400
300
200
100
0
ns
ns
***
****
*
**
*
YFP +
YFP -
YFP +
YFP -
SCI
Conditioning Lesion
cre^{+}Pfn1$^{wt/wt}$
cre^{+}Pfn1$^{fl/fl}$

Figure 3. Pfn1 depletion in vivo decreases axon regeneration and functional recovery. (**A**) Neuronal Thy1 promoter drives Cre recombinase and YFP expression in cre^{+}Pfn1 mice after tamoxifen administration, leading to *Pfn*1 exon1 excision. (**B**) βIII-tubulin staining of cre^{+}Pfn1 adult DRGs in the presence or absence of a shRNA Pfn2-expressing plasmid. Scale bar: 50 µm. (**C**) Total neurite length and (**D**) branching analysis related to (B). Only YFP^{+} (Pfn1 KO) neurons were quantified. Data represent mean ± SEM (**P < 0.01, ***P < 0.001, ****P < 0.0001, ns: not significant; (C): one-way ANOVA Tukey's posttest; (D): two-way ANOVA Tukey's posttest, *n* = 4-5 independent samples/condition; 5-35 neurons/sample). (**E**) Strategy to assess PNS regeneration. (**F**) PPD-stained sciatic nerves from cre^{+}Pfn1 mice, 7/15 days post-injury (PI). Scale bar: 20 µm. (**G**) Myelinated axon density related to (F). Data represent mean ± SEM (**P < 0.01, ns: not significant, t-test, *n* = 3-8 animals/condition). (**H**) 3D surface-rendered reconstructions of fluorescent-labeled NMJs with bungarotoxin. Scale bar: 50 µm. (**I**) zoom-ins of (H). Scale bar: 10 µm. (**J**) Volume quantification of NMJs (28 days PI). Data represent mean ± SEM (**P < 0.01, t-test, n = 3 animals/condition). (**K**) Motor nerve conduction velocity (28 days PI). Data represent mean ± SEM (**P < 0.01, t-test, *n* = 4-6 animals/condition). (**L**) Strategy to assess CNS regeneration. (**M**) YFP^{+}(green)/CT-B^{+}(red) axons (arrowheads) in spinal cord following SCI in cre^{+}Pfn1$^{wt/wt}$ and CL in either cre^{+}Pfn1$^{wt/wt}$ or cre^{+}Pfn1$^{fl/fl}$ mice. Scale bar: 50 µm; dashed line: lesion border; *r*:rostral, *c*:caudal, *d*:dorsal, *v*:ventral. (**N**) Quantification of mean growth distance of YFP^{+} (Pfn1 KO) and YFP^{-} ascending sensory axons (CT-B^{+} axons) from the rostral end of the injured dorsal column tract. Data represent mean ± SEM (*P < 0.05, **P < 0.01, ***P < 0.001, ****P < 0.0001, *n* = 4-5 animals/condition).

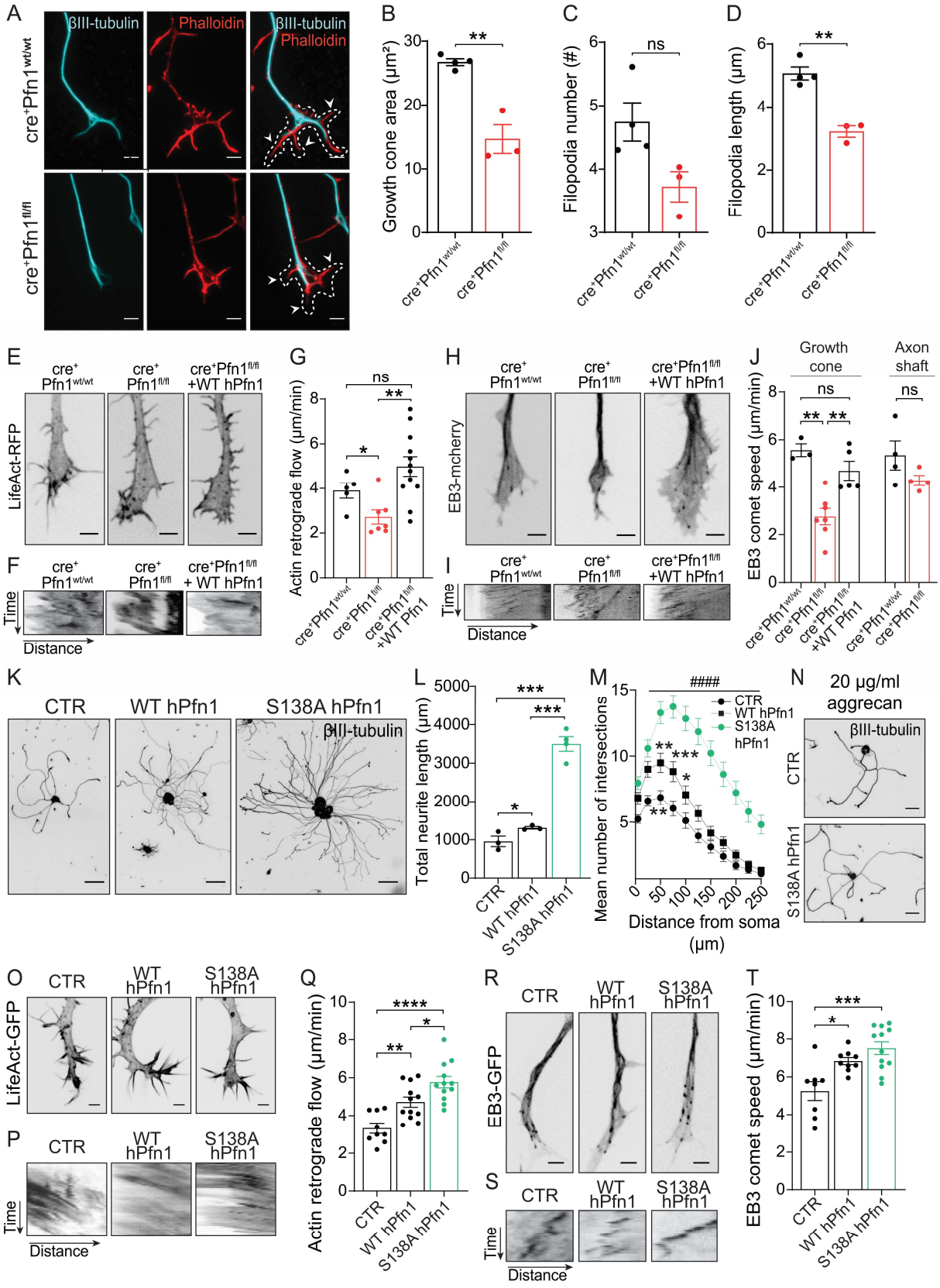

Figure 4. Pfn1 regulates actin and MT dynamics in growth cones. (**A**) βIII-tubulin (cyan) and actin (red) in cre⁺Pfn1 DRG growth cones. Scale bar: 3 µm; dashed line: cone area; arrowheads: filopodia. (**B**) Growth cone area, (**C**) filopodia number and (**D**) length related to (A). Data represent mean ± SEM (**P < 0.01, ns: not significant, t-test, *n* = 32-40 neurons/animal, 3-4 animals/condition). (**E**) LifeAct-RFP in cre⁺Pfn1 DRG growth cones.

Scale bar: 3µm. (**F**) Kymographs and (**G**) actin flow quantification related to (E). Data represent mean ± SEM (*P < 0.05, **P < 0.01, ns: not significant, *n* = 5-12 filopodia/condition; representative of 3-4 growth cones/condition. (**H**) EB3-mcherry in cre^{+}Pfn1 DRG growth cones. (**I**) Kymographs and (**J**) EB3 speed quantification related to (H) in growth cones and shaft. Data represent mean ± SEM (**P < 0.01, ns: not significant, one-way ANOVA Tukey's posttest, *n* = 3-7 growth cones/condition). (**K**) βIII-tubulin in WT and S138A hPfn1 DRGs. Scale bar: 80 µm. (**L**) Total neurite length and (**M**) branching related to (K). (L) and (M), data represent mean ± SEM; (L): *P < 0.05 and ***P < 0.001, *n* = 3-4 independent samples/condition; 13-31 neurons/sample; (M): *P < 0.05, **P < 0.01, ***P < 0.001 refers to CTR versus WT hPfn1; ####P < 0.0001 refers to CTR versus S138A hPfn1; two-way ANOVA Tukey's posttest. (**N**) βIII-tubulin in S138A hPfn1 DRGs cultured in aggrecan. Scale bar: 50 µm. (**O**) LifeAct-GFP, (**P**) kymographs and (**Q**) actin flow quantification in growth cones related to (K). (**R**) EB3-GFP, (**S**) kymographs and (**T**) EB3 speed quantification in growth cones related to (K). (O) and (R), scale bar: 3 µm. (Q) and (T), data represent mean ± SEM (*P < 0.05, **P < 0.01, ***P < 0.001, ****P < 0.0001, one-way ANOVA Tukey's posttest, *n* = 8-12 growth cones/condition).

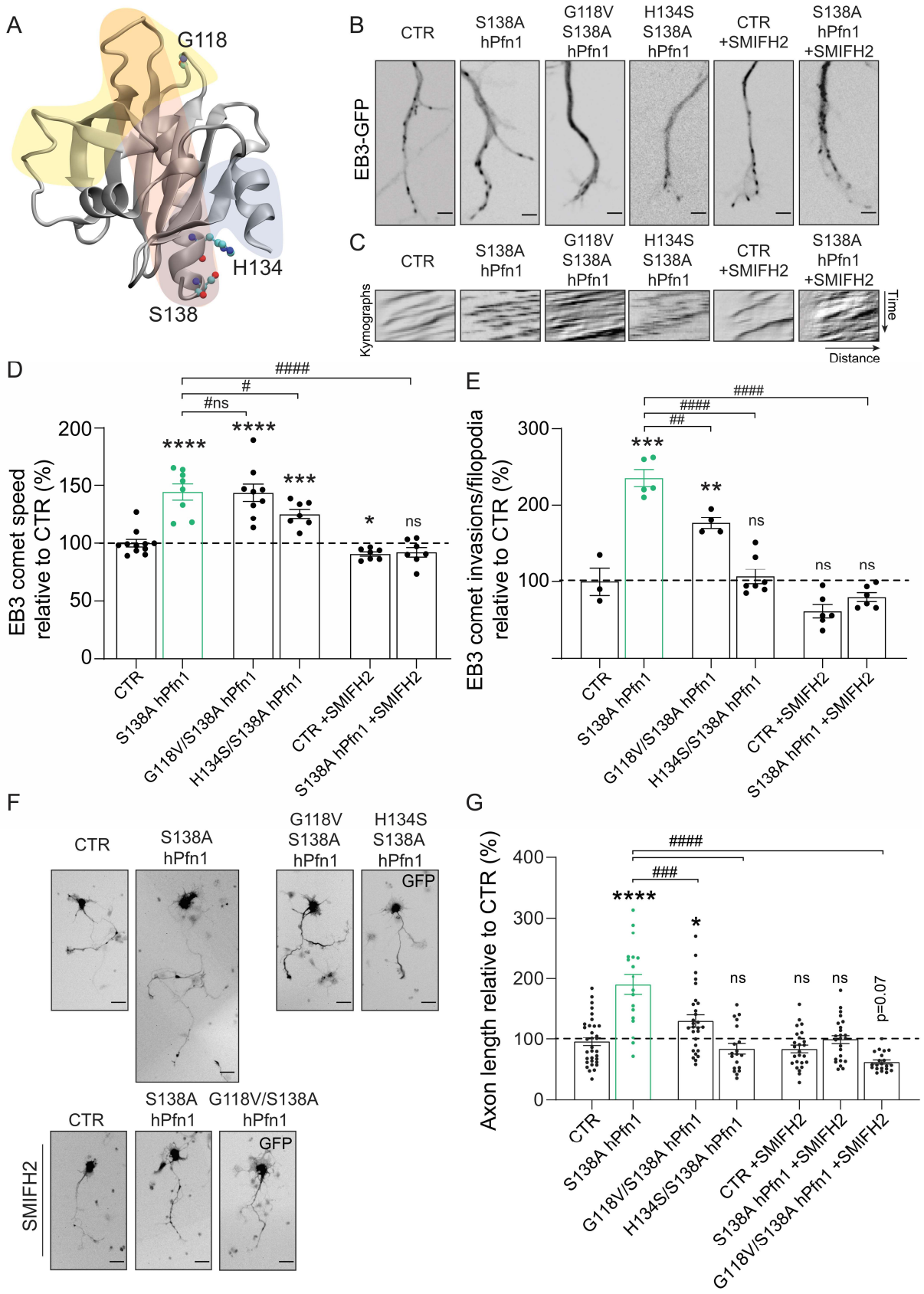

1

2 **Figure 5. S138A Pfn1 enhances MT dynamics via direct MT binding and formins.** (**A**)
3 Crystal structure of hPfn1 (PDB code: 1cf0). Residues G118 (MT-binding), H134 (poly-
4 proline-binding) and S138 (ROCK phosphorylation site, mediating inactivation of Pfn1-related
5 functions) are highlighted. Actin-, poly-proline- and PI(4,5)P2-binding regions of Pfn1 are

shadowed in light yellow, grey and red, respectively (adapted from (66)). (**B**) Live-cell imaging of EB3-GFP in hippocampal neurons transfected with EB3-GFP and either a control empty vector (CTR) or plasmids expressing S138A hPfn1 or S138A Pfn1 mutants (G118V/S138A or H134S/S138A hPfn1); CTR and S138A hPfn1 treated with SMIFH2 are also shown. Scale bar: 2 µm. (**C**) Kymographs related to (B). (**D**) Analysis of MT growth speed and (**E**) EB3 comet invasion frequency per filopodia. In (D) and (E), data represent mean ± SEM (*P < 0.05, **P < 0.01, ***P < 0.001, ****P < 0.0001, ns: not significant in relation to CTR and $^{\#}$P < 0.05, $^{\#\#}$P < 0.01, $^{\#\#\#\#}$P < 0.0001, $^{\#}$ns: not significant in relation to S138A hPfn1; in (D): *n* = 7-11 and in (E): n= 3-7 growth cones/condition). (**F**) GFP^{+} hippocampal neurons transfected with either a control empty vector (CTR) or plasmids expressing different hPfn1 mutants, either untreated or treated with SMIFH2, whenever indicated. Scale bar: 30 µm. (**G**) Quantification of axon length related to (F). Data represent mean ± SEM (*P < 0.05, ****P < 0.0001, ns: not significant in relation to CTR, and $^{\#\#\#}$P < 0.001 and $^{\#\#\#\#}$P < 0.0001 in relation to S138A hPfn1, one-way ANOVA Tukey's posttest, n=18-33 neurons/condition; representative of 3-5 independent experiments/condition).

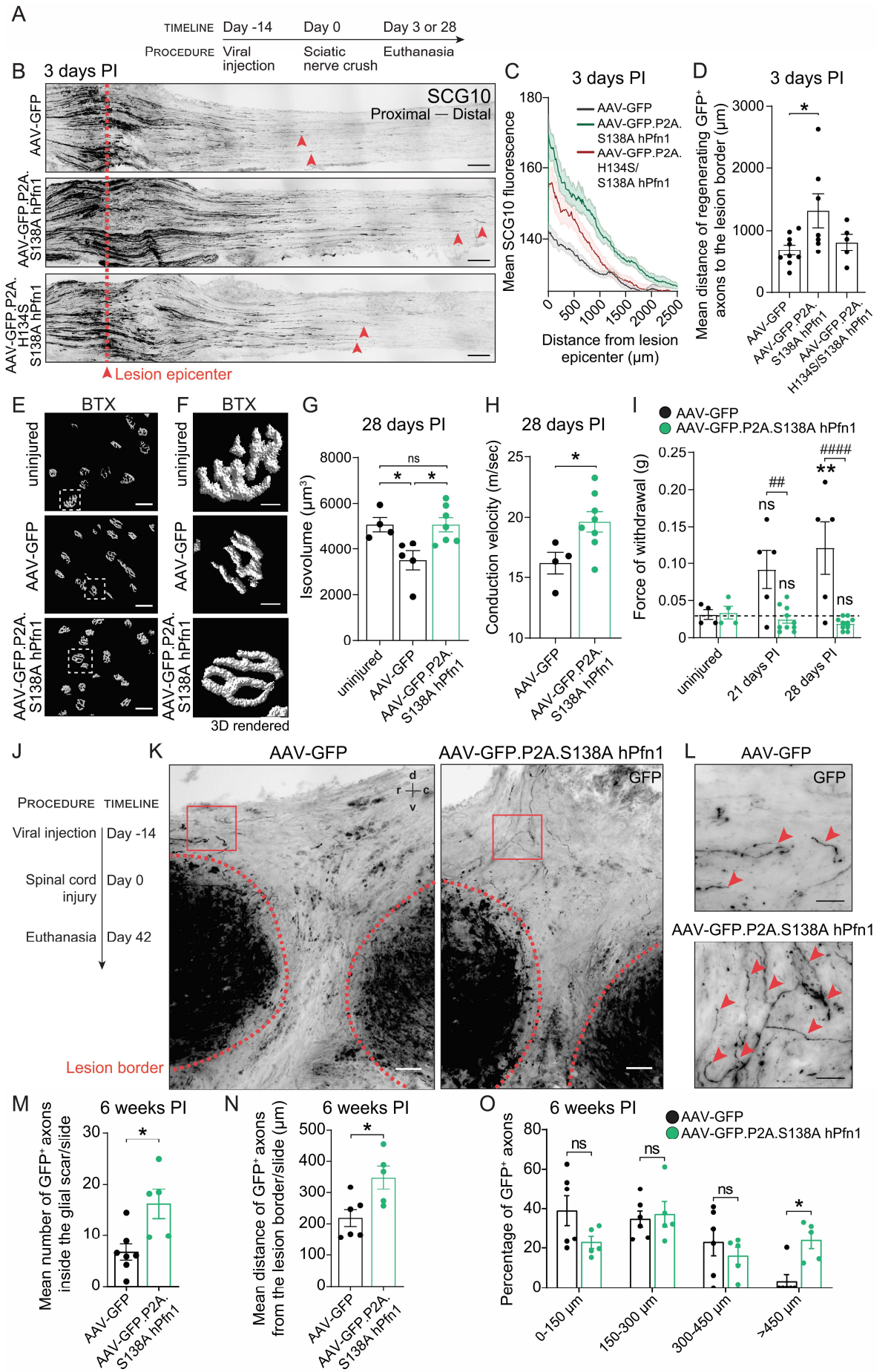
A
TIMELINE Day -14 Day 0 Day 3 or 28
PROCEDURE Viral injection Sciatic nerve crush Euthanasia
B 3 days PI
SCG10
Proximal — Distal
AAV-GFP
AAV-GFP.P2A. S138A hPfn1
AAV-GFP.P2A. H134S S138A hPfn1
Lesion epicenter
C 3 days PI
Mean SCG10 fluorescence
AAV-GFP
AAV-GFP.P2A. S138A hPfn1
AAV-GFP.P2A. H134S/ S138A hPfn1
Distance from lesion epicenter (µm)
D 3 days PI
Mean distance of regenerating GFP+ axons to the lesion border (µm)
E BTX
F BTX
uninjured
AAV-GFP
AAV-GFP.P2A. S138A hPfn1
3D rendered
G 28 days PI
Isovolume (µm3)
H 28 days PI
Conduction velocity (m/sec)
I
AAV-GFP
AAV-GFP.P2A.S138A hPfn1
Force of withdrawal (g)
uninjured
21 days PI
28 days PI
J
PROCEDURE TIMELINE
Viral injection Day -14
Spinal cord injury Day 0
Euthanasia Day 42
K AAV-GFP
AAV-GFP.P2A.S138A hPfn1
GFP
Lesion border
L AAV-GFP
AAV-GFP.P2A.S138A hPfn1
M 6 weeks PI
Mean number of GFP+ axons inside the glial scar/slide
N 6 weeks PI
Mean distance of GFP+ axons from the lesion border/slide (µm)
O 6 weeks PI
Percentage of GFP+ axons
0-150 µm
150-300 µm
300-450 µm
>450 µm

Figure 6. In vivo delivery of S138A hPfn1 elicits regeneration of peripheral and CNS axons. (**A**) Strategy to assess peripheral regeneration following viral delivery of S138A hPfn1. (**B**) SCG10 staining of longitudinal sciatic nerve sections at 3 days PI; red dashed lines indicate the lesion epicenter; red arrowheads highlight regenerating axons. Scale bar: 200 µm. (**C**) SCG10 fluorescence versus distance to lesion epicenter. (**D**) Mean distance of GFP^+ sciatic nerve axons regenerating distally to the lesion edge 3 days PI. Data represent mean ± SEM (*P < 0.05, *n* = 5-9 animals/condition). (**E**) 3D surface-rendered reconstructions, (**F**) zoom-in of (E) and (**G**) volume quantification of fluorescent-labeled NMJs with bungarotoxin (BTX), 28 days PI. Scale bar (E): 50 µm; scale bar (F): 10 µm. (**H**) Motor nerve conduction velocity, 28 days PI. In (G) and (H), data represent mean ± SEM (*P < 0.05, ns: not significant, t-test, *n* = 4-8 animals/condition). (**I**) Von Frey Hair test, 21/28 days PI. Data represent mean ± SEM (**P < 0.01 and ns: not significant are related to AAV-GFP uninjured condition, $^{\#\#}P < 0.01$ and $^{\#\#\#\#}P < 0.0001$ refers to AAV-GFP versus AAV-GFP.P2A.S138A hPfn1 animals, two-way ANOVA Sidak's posttest, *n* = 5-10 animals/condition). (**J**) Strategy to assess CNS regeneration following delivery of AAV-GFP and AAV-GFP.P2A.S138A hPfn1. (**K**) Injured spinal cords 6 weeks following transection. Scale bar: 100 µm; red dashed line: lesion border; arrowheads: GFP^+ axons within the lesion core; *r*:rostral, *c*:caudal, *d*:dorsal, *v*:ventral. (**L**) Zoom-ins of (K). Scale bar: 40 µm. (**M**) Number of GFP^+ axons regenerating within the glial scar. (**N**) Distance (rostral to caudal) of regenerating axons and (**O**) percentage of GFP^+ axons at different distance ranges from the injury border. Data represent mean ± SEM (*P < 0.05, **P < 0.01, ns: not significant, t-test, *n* = 5-7 animals/condition).